Investigation of thermo-magnetic instability in superconducting NbN thin-films by automated real-time magneto-optical imaging.

by

Karl E. Eliassen

THESIS

for the degree of

Master of Science

in Condensed Matter Physics

Faculty of Mathematics and Natural Sciences
University of Oslo

September 2008

Det matematisk- naturvitenskapelige fakultet
Universitetet i Oslo

Abstract

If a magnetic field above a certain critical field B_{c1} is imposed on a type II superconductor, it will start to penetrate in the form of magnetic flux quanta, or vortices, resulting in a meta-stable non-equilibrium critical state. The critical state can collapse due to thermo-magnetic instability in the superconductor, resulting in a sudden large scale redistribution of vortices. This might cause the superconductor to heat up to above the critical temperature, at least locally, where sudden resistivity can have catastrophic consequences.

In this thesis we have studied thermo-magnetic instability in superconductor thin-films, in a wide range of fields and temperatures, by automating the experimental setup and developing algorithms for graphical recognition of flux avalanches, and determination of threshold fields for the formation of these avalanches.

When constructing a phase diagram of the threshold fields as a function of temperature we found a hysteretic behaviour of the upper thresholds for increasing and decreasing magnetic fields. An explanation is given based on a theoretical model of the correlation between the threshold field and the critical current density. We also found that sufficiently large primary avalanches have the ability to move independently of the shielding current inside of the flux front. At decreasing fields we observed secondary avalanches starting at the zero-field d-line. Heat from a primary avalanche reduce the pinning force, which in some locations will let the Lorentz force overcome the pinning and move vortices. This create a local instability that can sometime trigger a secondary avalanche.

Acknowledgements

After "living" in office 106a with the Superconducting group for almost 2.5 years, 2 of those as a master student, I wish to thank the following:

My supervisor Tom Henning Johansen for accepting me as his student, and letting me dig deeper into the field of superconductivity, which have intrigued me for 20 odd years, and for good advice and suggestions toward the end of my thesis.

My co-supervisor Vitaliy Yurchenko for sharing his knowledge of superconductivity, and how to extract their secrets using magneto-optical imaging

Joakim Bergli for taking the time to help me with all kind of physics and mathematics problems during the last 2.5 years.

Martin and Aurora for daily help and advise.

The rest of the group, you are too many to mention, for making the stay here interesting and informative, both professionally and socially.

A special thanks to my wife Gunn, for her encouragement and support throughout my studies, and for falling quietly and unnoticeable asleep at night when I try to explain the joys of physics. And my daughter Erika for brightening up the darkest days.

I also have to mention the lunchroom, where the rest of the worlds problems was solved, and the all important coffee machine. The true force behind the success of the AMCS group. As Louis XV expressed it: "What would life be without coffee? But then, what is it with coffee?".

Last but not least a big thank to "System of a down" for helping me process my frustrations and aggravations during my master studies. B.Y.O.B.!

Thank you!

Contents

1 Introduction **1**

1.1 Superconductivity . . . 2
1.1.1 History . . . 2
1.1.2 Zero resistivity . . . 3
1.1.3 Perfect diamagnetism . . . 4
1.1.4 Critical field and critical current density . . . 6
1.1.5 Ginzburg-Landau theory, and the fundamental length-scales ξ and λ_L . . . 7
1.1.6 Type I and type II superconductors . . . 9
1.1.7 Abrikosov vortices, flux quantum and pinning . . . 11
1.2 Critical state . . . 13
1.2.1 The Bean model . . . 13
1.2.2 Critical state for thin-film superconductors . . . 16
1.3 Thermo-magnetic instability . . . 20
1.4 Outline . . . 21

2 Experimental methods and setup **23**

2.1 Magneto-optical imaging (MOI) . . . 23
2.1.1 Faraday rotation . . . 24
2.1.2 The MOI-technique . . . 25
2.1.3 Magneto-optical film . . . 25
2.2 Instrumentation . . . 27
2.2.1 Magneto-optical imaging setup . . . 27
2.3 The samples . . . 29
2.4 Data acquisition by LabView . . . 30

3 Results and discussion **31**

3.1 Distribution of the magnetic flux in NbN . . . 31
3.2 Automation of the experimental setup . . . 34
3.2.1 CEFA4.vi . . . 38

3.2.2 Algorithm for graphical recognition of magnetic flux avalanches 41
3.3 Phase diagram 44
3.4 Flux dynamics 48
3.4.1 Size of flux jumps 48
3.4.2 Large flux avalanches 50
3.4.3 Secondary avalanches crossing d-lines 53

4 Concluding remarks **55**

A LabView **57**

B Matlab code **63**
B.1 dendrites.m 63
B.2 finddend.m 65

Bibliography **71**

Chapter 1

Introduction

Some materials have the property that when cooled below a certain critical temperature (T_c) they become superconducting. A superconductor have no resistivity and expels magnetic fields. If a magnetic field is slowly imposed on a so-called type II superconductor, flux will, if the field is stronger than a certain critical field (B_{c1}), start to penetrate into the superconductor. Lorentz force will push them further into the superconductor while pinning force due to structural irregularities will hold them back. This results in a meta-stable non-equilibrium critical state, where the density of flux is highest on the edge. Under certain conditions this critical state can collapse due to thermally driven flux jumps, resulting in a sudden large scale redistribution of flux. This might lead the superconductor to heat up to above the critical temperature, at least locally, where sudden resistivity can have catastrophic consequences. In most cases the superconductor cools down again and a new meta-stable state is formed.

This chapter gives a short general introduction to the field of superconductivity including the Ginzburg-Landau theory and Abrikosov-vortices, and finish off with the topics critical state model and thermo-magnetic instability, which are important for this thesis.

1.1 Superconductivity

1.1.1 History

This thesis will not go into detail about the history of superconductivity, it can easily be found in many books, e.g. Fossheim and Sudboe [1] and Tinkham [2], and on numerous Internet web-sites, e.g. http://superconductors.org/History.htm. We will limit this section to the two most important discoveries in superconductivity, the first made possible by a scientists own Nobel prize discovery, the second giving the scientists the "fastest Nobel prize in history" (in physics).

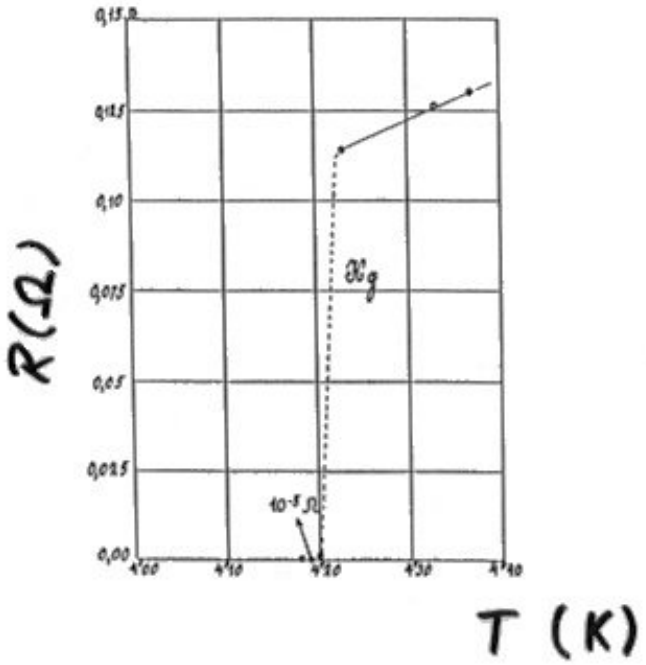

Figure 1.1: Kamerlingh-Onnes original graph of the resistance of mercury versus absolute temperature [3]

In 1911 Heike Kamerlingh Onnes used his discovery of how to liquefy Helium [4], to cool down mercury (Hg). He wanted to see if the DC resistivity of metals would steadily decrease with lower temperatures, and eventually drop to nil at zero Kelvin. What he found was that resistivity of mercury really

did reduce linearly, until it abruptly dropped to zero at 4.2 K [3], the critical temperature (T_c) of mercury (figure 1.1). He called this phenomena "supra-conductivity", but later adopted the term of "superconductivity". In the years to come he found that superconductors also have a critical field (B_c) and a critical current density (J_c),which will be explained below. He later received the Nobel prize in physics "For his investigations on the properties of matter at low temperatures which led, inter alia, to the production of liquid helium"[1].

75 years later, in 1986, high-T_c superconductivity was discovered by Bednorz and Müller [5]. Before this many physicist believed that current theories about superconductivity forbade the existence of superconductors with a critical temperature of more than 30 K. But superconductivity in a lanthanum-based cuprate perovskite material $Ba_xLa_{5-x}Cu_5O_{5(3-y)}$ was found at T~35 K, though being a record high T_c, it still needed liquid helium (LHe) as a coolant. However, this discovery triggered a long range of new discoveries, and within a year the record of the highest T_c was increased by an incredible 60 degrees (to 93 K), by Wu et.al. [6], with one of the most widely used superconductors since; $YBa_2Cu_3O_{7-\delta}$ (YBCO). Now it was sufficient to use the less expensive liquid nitrogen (LN) as a cryo-coolant. The progression of highest known T_c during last century can be found in figure 1.2.

1.1.2 Zero resistivity

Onnes found that mercury loses its electrical resistance abruptly (see figure 1.1) as far as his instruments could see, but still believed that there was some micro resistance in the metal. Zero resistivity also means infinite conductivity, unfortunately they are equally difficult to measure because of the limitations of the measuring devices.

There is however a way to indirectly measure resistivity, or at least confine it to a maximum value, where time is a limiting factor of how low resistivity one can measure [1]. Many investigators have used the method called persistent current, which is to induce a current in a superconducting ring and monitor the associated magnetic field (figure 1.3). By using Kirchhoff's second law, stating that the algebraic sum of the potential differences in any loop must equal zero, we reach the equation

$$LI' + RI = 0 \tag{1.1}$$

[1] http://www.kva.se/KVA_Root/swe/awards/nobel/index.asp

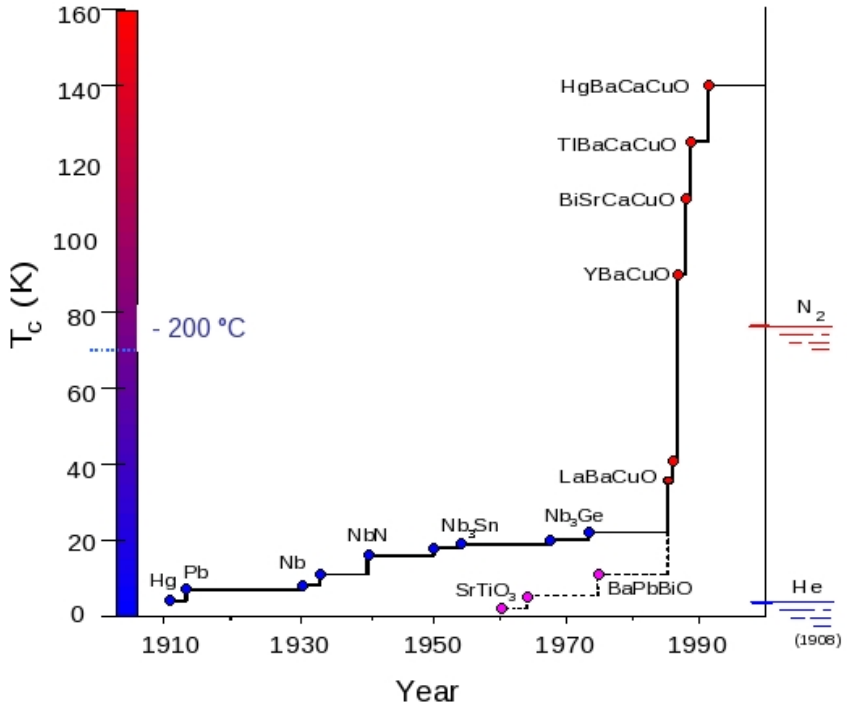

Figure 1.2: Record high critical temperatures (T_c) and the year of discovery [7]

By solving this for I(t)

$$I(t) = I_0 e^{-\frac{t}{\tau}} \qquad \tau = \frac{L}{R} \tag{1.2}$$

they calculated the relaxation time (t) of the system. If the magnetic field has not decreased (as will be expected for a superconductor), they can by considering the limitations of the measuring devices find a maximum resistance of the superconductor.

Among those who have done this are Kedves et.al.[8], who found when observing an YBCO ceramic superconductor at liquid nitrogen temperatures for 12 days($\sim 10^6\ s$), an upper limit of $7 \cdot 10^{-25}\ \Omega m$. For comparison it is a minimum of 15 orders of magnitude less than for a similar ring made of copper at 80 K ($\approx 2 \cdot 10^{-9}\ \Omega m$), and can be regarded as zero resistivity.

1.1.3 Perfect diamagnetism

In 1933 Walther Meissner and Robert Ochsenfeld made the discovery of perfect diamagnetism in superconductors. They observed that if a superconduc-

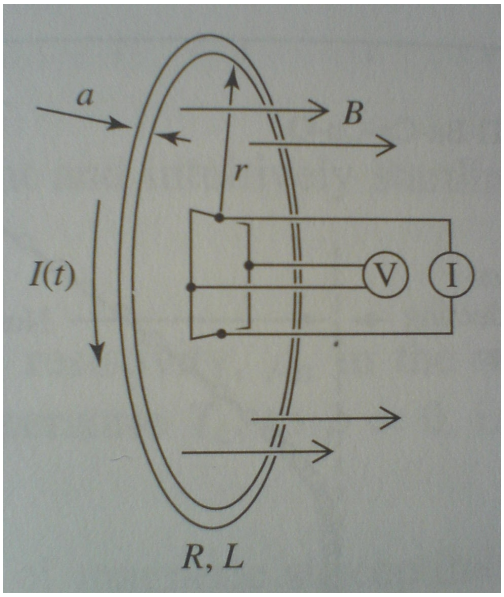

Figure 1.3: Sketch of a simple setup to monitor the possible decay of current via its associated magnetic induction in a closed loop [1]

tor is cooled down (zero field cooling: ZFC) and then placed in a magnetic field, the field will be excluded. Moreover, if a superconductor in it's normal state is imposed with a magnetic field, and then cooled down to below T_c (field cooling: FC), the magnetic field is expelled from the superconductor. This expulsion is called the Meissner effect [9]. Since there is no magnetic field (B) inside the superconductor, the magnetic field strength (H) but in the opposite direction.

$$B = \mu_0(\mathbf{H} + \mathbf{M}) = 0 \tag{1.3}$$

$$\Rightarrow \mathbf{M} = -\mathbf{H} \tag{1.4}$$

Magnetization is the response of a material to an applied magnetic field. The degree of magnetization is known as susceptibility (χ), and is defined as:

$$\chi = \frac{d\mathbf{M}}{d\mathbf{H}} \tag{1.5}$$

which in a superconductor is equal to -1, giving perfect diamagnetism.

The reason why the magnetic field is excluded/expelled from the superconductor, as seen in figure 1.4, is that a shielding current is generated inside the

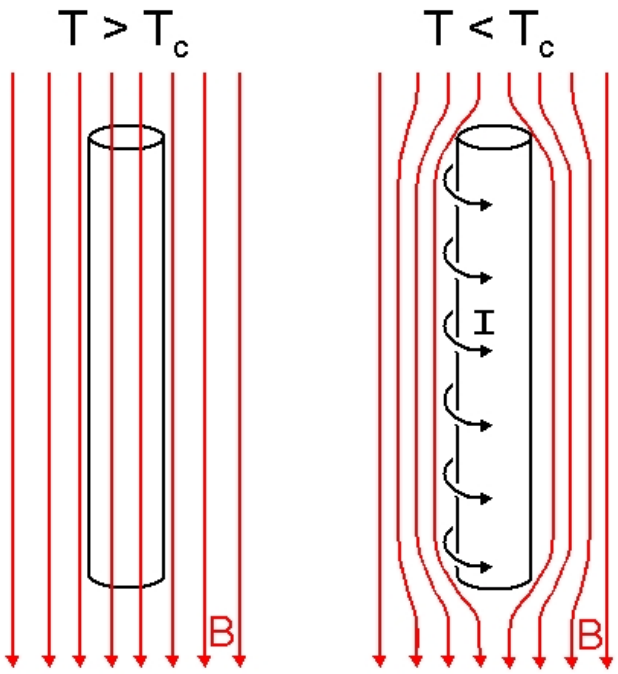

Figure 1.4: Meissner effect, the expulsion of a magnetic field from a superconducting rod [10]

superconductor which induce a magnetization (M) in the opposite direction of the applied field, and cancel it out.

1.1.4 Critical field and critical current density

There are three parameters that can destroy superconductivity, the first one is as mentioned above temperature. If temperature is increased to above T_c, the material will transform back to it's normal state. The second parameter is the magnetic field. As the applied magnetic field is increased, so will the shielding current. The current will be flowing near the surface of the superconductor, making it more natural to talk about current density. At a critical magnetic field (B_c) the shielding current density will have reached it's maximum in the superconductor, and the magnetization will eventually be weaker than the applied field. When this happens, the superconductivity will be destroyed.

If we send a current through the superconductor, also called a transport current, it will induce a magnetic field. When the total current density reaches

a certain value, namely the critical current density J_c, the induced B-field is so strong that superconductivity is destroyed, this is known as Silsbee's rule.

The critical temperature, field and current density are all affected by the two other parameters. If you increase the applied magnetic field, this will lower the critical current density and temperature (see figure 1.5).

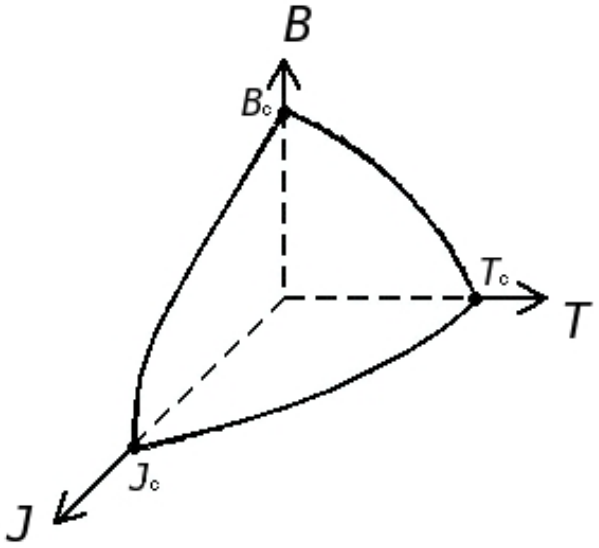

Figure 1.5: Generic phase diagram showing the relationship between critical temperature (T_c), critical field (B_c) and critical current density (j_c)

1.1.5 Ginzburg-Landau theory, and the fundamental length-scales ξ and λ_L

The thermodynamic properties of a superconductor can be described in terms of Gibbs free energy density, where the transition between normal and superconducting state can be seen as a second order phase transition. The superconducting state can be characterized by a complex order parameter $\psi = |\psi|e^{i\phi}$, where $|\psi|^2 = n_s^*$ is the density of superconducting charge carriers later known as Cooper-pairs, which is zero when $T > T_c$ and non-zero when $T < T_c$. Ginzburg and Landau assumed [11] [2] that close to, but below the critical temperature (T_c), the free energy density can be expanded in powers of $|\psi|^2$, see eqn.1.6. By minimizing this with respect to the variations

in the order parameter (ψ) and the vector potential (A) one arrives at the Ginzburg-Landau equations (GL1: eqn.1.7 and GL2: eqn.1.8):

$$f = f_n + \alpha|\psi|^2 + \frac{\beta}{2}|\psi|^4 + \frac{1}{2m^*}\left|(-i\hbar\nabla - e^*\mathbf{A})\,\psi\right|^2 + \frac{|\mathbf{B}|^2}{2\mu_0} \tag{1.6}$$

$$0 = \alpha\psi + \beta|\psi|^2\psi + \frac{1}{2m^*}(-i\hbar\nabla - e^*\mathbf{A})^2\psi \tag{1.7}$$

$$\mathbf{j} = \frac{i\hbar e^*}{2m^*}(\psi^*\nabla\psi - \psi\nabla\psi^*) - \frac{e^{*2}}{m^*}\mathbf{A}|\psi^2| \tag{1.8}$$

m^*, e^* and n^* are the (effective) mass, charge and density of the superconducting charge carriers, related to ordinary electrons by:

$$\begin{aligned} m^* &= 2m \\ e^* &= \pm 2e \\ n_s^* &= \frac{1}{2}n_s \end{aligned}$$

α and β are functions of the temperature, and while β is always positive, α can be both positive and negative. If $\alpha > 0$ minimum free energy will occur at $|\psi|^2 = 0$, corresponding to a normal state since there are no superconducting charge carriers. But if $\alpha < 0$, we will have minimum at $|\psi|^2 = |\psi_\infty|^2 = \frac{|\alpha|}{\beta}$, where $|\psi_\infty|$ is the modulus of the order parameter infinitely far into the superconductor. Since the system is equilibrating at the minimum free energy density where $|\psi|^2 \neq 0$, we have a superconducting state (figure 1.6).

By considering a simplified case of zero-field close to the superconductor boundary (A=0), Ginzburg and Landau found a characteristic length scale ξ eqn.1.9. Only within this length scale from the superconductor boundary can the order parameter alter significantly, further in the free energy is at it's minimum and we have the maximum number of superconducting charge carriers.

From eqn.1.8 they also derived the penetration depth λ_L eqn.1.10, first introduced by the London brothers in 1935 [12], which describes how far into the superconductor an applied magnetic field will penetrate.

$$\xi = \sqrt{\frac{\hbar^2}{2m^*|\alpha|}} \tag{1.9}$$

$$\lambda = \sqrt{\frac{m^*\beta}{\mu_0 e^{*2}|\alpha|}} \tag{1.10}$$

$$\kappa = \frac{\lambda}{\xi} \tag{1.11}$$

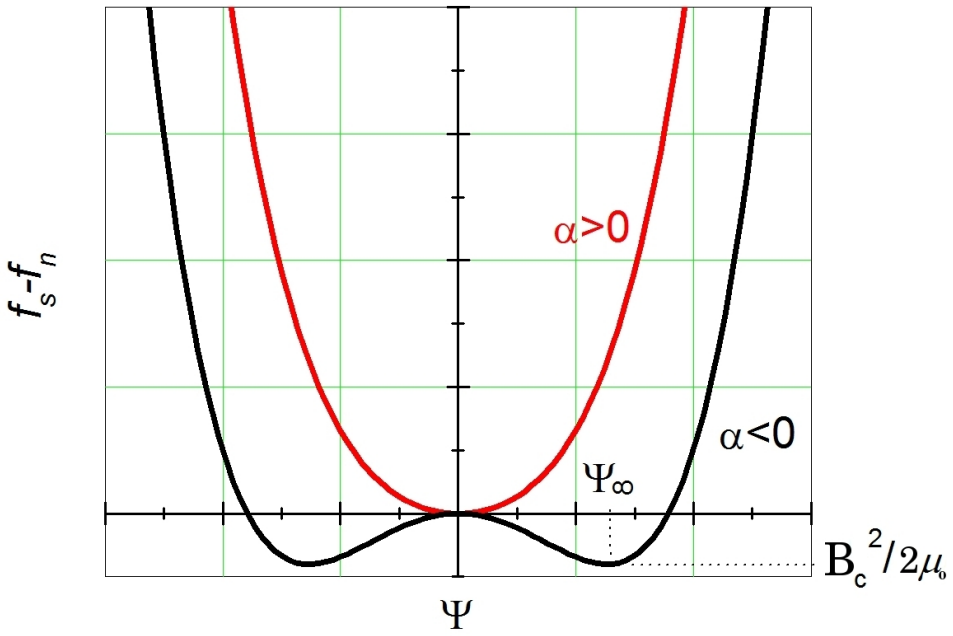

Figure 1.6: Difference between the Gibbs free energy density in the superconducting ($\alpha < 0$) and normal ($\alpha > 0$) state, depending on the order parameter in the Ginzburg-Landau theory.

These two length scales can be combined into the Ginzburg-Landau parameter κ eqn.1.11. With the help of these length scales they found that the domain-wall surface energy of the superconductor was positive for $\kappa < \frac{1}{\sqrt{2}}$ and negative for $\kappa > \frac{1}{\sqrt{2}}$. They anticipated that one would have an intermediate state between the normal and superconducting state when $\kappa < \frac{1}{\sqrt{2}}$, involving partial penetration of an applied field into the specimen giving a partial transition to the normal state, see figure 1.7.

1.1.6 Type I and type II superconductors

Superconductors can be divided into two principal categories, type I when $\kappa < \frac{1}{\sqrt{2}}$ and and type II $\kappa > \frac{1}{\sqrt{2}}$. The two types will behave very similar with respect to resistivity and the Meissner state as long as the applied field is low. The behaviour of a type I superconductor at high fields are described

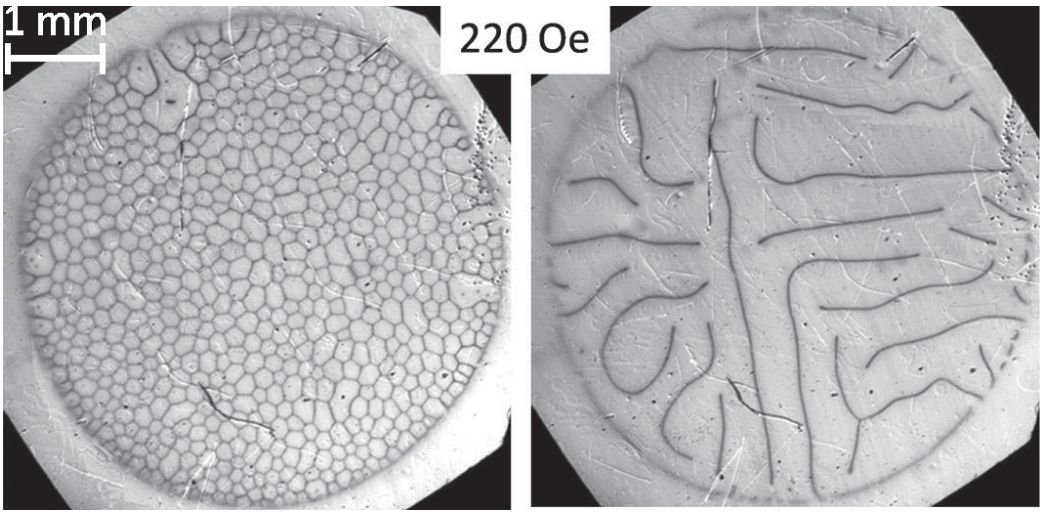

Figure 1.7: Structure of the intermediate state in a disc-shaped Pb single crystal at T=5 K, B_{app}=22 mT. Left column; increasing magnetic field after ZFC. Right column; decreasing field, Prozorov et.al [13]

above. In a type II superconductor magnetic flux will partially penetrate the superconductor. This is called a mixed state.

If a transport current is imposed on the superconductor, a Lorentz force $\mathbf{J} \times \mathbf{\Phi_0}$ will move the magnetic flux with a velocity v_ϕ from one side of the superconductor to the other, perpendicular to the current direction [14]. The moving magnetic flux will generate an electric field $\mathbf{E}$ in the superconductor perpendicular to both $\mathbf{v}_\phi$ and $\mathbf{B}$

$$\mathbf{E} = \mathbf{v}_\phi \times \mathbf{B} \tag{1.12}$$

This gives an ohmic loss: $\mathbf{J} \cdot \mathbf{E}$.

But superconductors are never perfect, there are defects like impurities, voids, spatial inhomogeneities etc. These defects act like pinning sites for the magnetic flux, and as long as the pinning force of the pinning site is stronger than the Lorentz force of the magnetic flux, it will be trapped. The stronger the pinning force, the higher transport current can be imposed, or B-field applied on the superconductor without overcoming the pinning force.

1.1.7 Abrikosov vortices, flux quantum and pinning

While Ginzburg and Landau had predicted the intermediate state of type I superconductors, Abrikosov [15] worked on situations where the domain-wall surface energy of the superconductor was negative ($\kappa > \frac{1}{\sqrt{2}}$). He predicted that when a strong enough field was applied to what he called a type II superconductor ($B_{app} > B_{c1}$), the negative surface energy would make it energetically favourable for the superconductor to increase the amount of domain-wall surface. It will therefore subdivide the normal state domain into cylindrical domains penetrating into the superconductor and containing a magnetic flux quantum. These quantized tubes or flux lines are called (Abrikosov-) vortices, where only the center of this vortex is in normal state, and shielding currents circulate on the outside. The radius of a vortex is equal to the coherence length of the material, and the flux quantum which is restricted inside a radius of the penetration depth can be calculated from the Ginzburg-Landau theory to be $\Phi_0 = \frac{h}{e^*}$, where h is Plancks constant.

The vortices will continue to penetrate more and deeper into the superconductor, and when the density is high they will form a hexagonal pattern in the superconductor, also called flux line lattice (figure 1.8). When the applied magnetic field reaches an upper critical field B_{c2}, where the density of the vortices is so high that the cores start to overlap (distance between them are less than ξ), superconductivity will be destroyed.

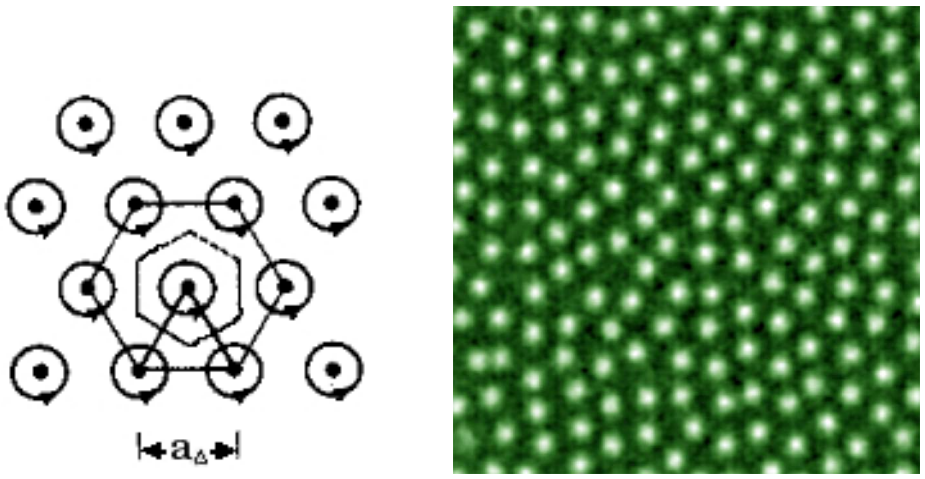

Figure 1.8: Schematic diagram of hexagonal vortex lattice (left), and magneto-optical images of vortex lattice in a $NbSe_2$ superconducting crystal at T=4.3 K after cooling in magnetic field of B=0.3mT by Goa et.al. ([16]).

1.2 Critical state

The pinning sites in a superconductor will cause it to have several irreversible properties, some of which are interpreted by the critical state model. A critical state is a meta-stable non-equilibrium state with regards to vortices driven into the superconductor by an applied field or current, not reaching their equilibrium position because of their interactions with defects in the crystal lattice [17]. The critical state model presumes that when a low applied magnetic field or a current that induce a field is imposed on a type II superconductor, it will, if the fields are stronger than B_{c1} start to penetrate the sample in the form of vortices. Due to pinning forces and repulsion between them, the vortices will form a flux density gradient with a maximum at the edge of the superconductor and a minimum (no vortices) the flux front. This is what we call a critical state, where both magnetic field and current density have certain values within the depth of the flux front. In the rest of the superconductor the magnetic field and current density will be zero. When the applied field or current is increased, the depth of the flux front will also increase.

1.2.1 The Bean model

Charles Bean was the first to elaborate on such a critical state model [18] [19]. For long cylindrical superconductors in a longitudinal applied field the Bean model postulates that the current density in this outer part of the superconductor, where magnetic flux has penetrated is constant and critical. Using the Maxwell equation $\nabla \times \mathbf{B} = \mu_0 \mathbf{J}$ this also gives a constant curl of the magnetic field within the specimen, inferring that the magnetic field changes linearly from the edge of the specimen through the depth of the flux front, see figure 1.9a. In his model Bean disregarded demagnetization effects, assumed that J_c was independent of the magnetic field and that $B_{c1} = 0$.

When increasing the magnetic field or transport current, the depth of the flux front will increase, but the current density in the flux front will stay the same since it is already critical (figure 1.9c). At one point the whole specimen will become filled with critical current density, and the magnetic field will reach the center of the specimen ($B_{app} = B^*$), where

$$B^* = \mu_0 J_c a \tag{1.13}$$

is the characteristic (full penetration) field, and a is the radius of the specimen. However, if we continue to increase the applied magnetic field, the magnetic field within the specimen will become stronger even though the

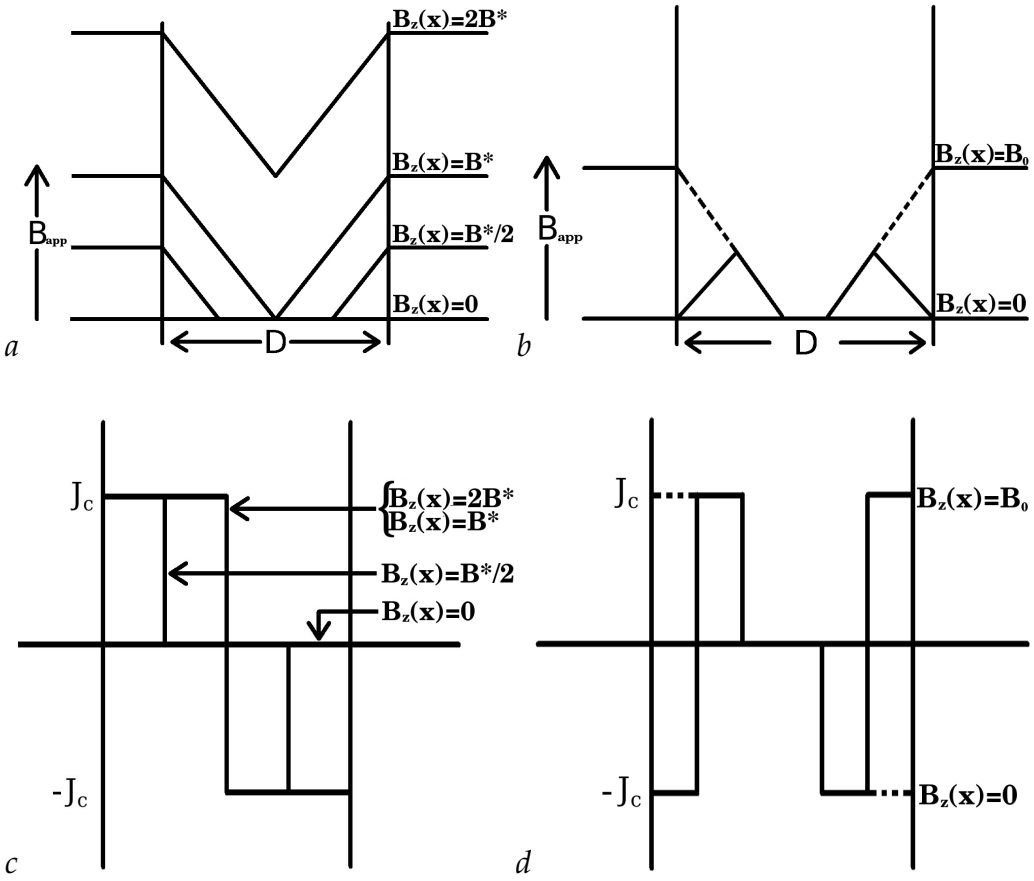

Figure 1.9: The Bean model [18], showing the dependence of the internal magnetic field $B_z(x)$ and critical current $J_y(x)$ on the applied magnetic field B_{app}

current density stays the same (figure 1.9a,c).

If we reverse the field, the curl of the magnetic field will change sign, but still be constant. The magnetic field within the specimen will decrease from the edges, leading to some flux being trapped in the superconductor (figure 1.9b,d). When we reach an applied field $B_{app} = -B^*$, all flux of positive polarity will be gone. By applying and reversing the fields a few times we trace out a hysteresis curve, showing the relation between applied field and magnetization in the superconductor, see figure 1.10.

There are several modifications to the critical state model, like the Kim model [20] [21], the fixed pinning model [22] [23] and the generalized model [24].

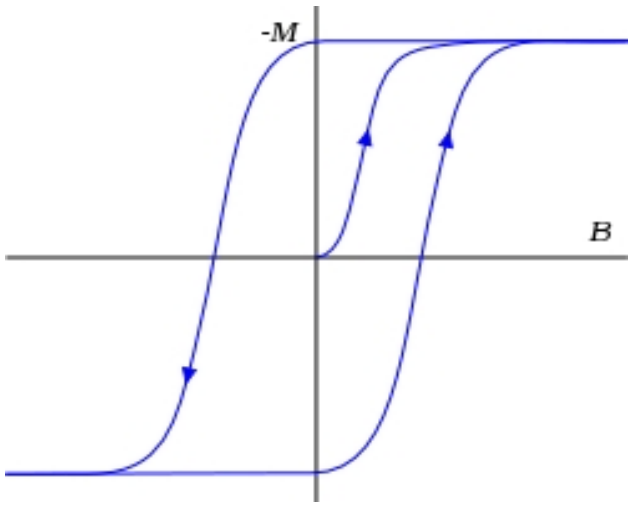

Figure 1.10: Hysteresis loop of magnetization (M) in the superconductor versus the applied magnetic field (B_{app})

1.2.2 Critical state for thin-film superconductors

In thin-film superconductors the current density will be distributed across the entire specimen, even at low applied magnetic fields. The magnetic flux will however only penetrate the sample within a flux front, as described by the critical state model [25]. The reason why current density is not zero on the inside of the flux front is the curvature of the magnetic field lines, giving a y-component of the magnetic field (see figure 1.11) on the surface, and both field and shielding current penetrate in the z-direction to a depth of λ_L. With films of thickness comparable to λ_L this gives a large current density

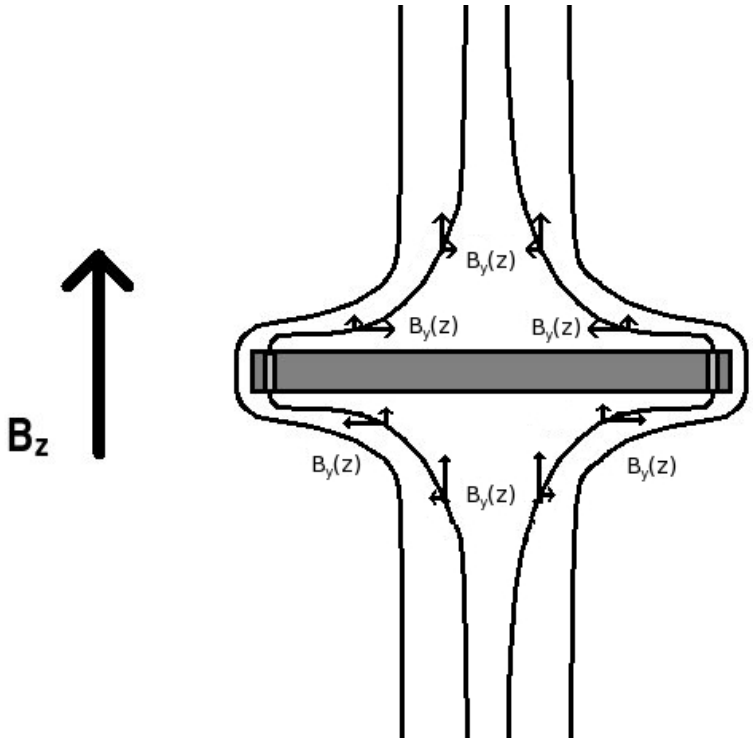

Figure 1.11: Magnetic field through a thin film superconductor at critical state, partly penetrated

in the flux free areas. We then have the current density distribution found in figure 1.12 for thin-film critical state model, which is quite different from the Bean model (figure 1.9) for bulk samples.

In the area where the flux lines have penetrated the current density will still be critical, and as the field is increased, the flux front will move towards the center of the superconductor, until the whole specimen has a critical current

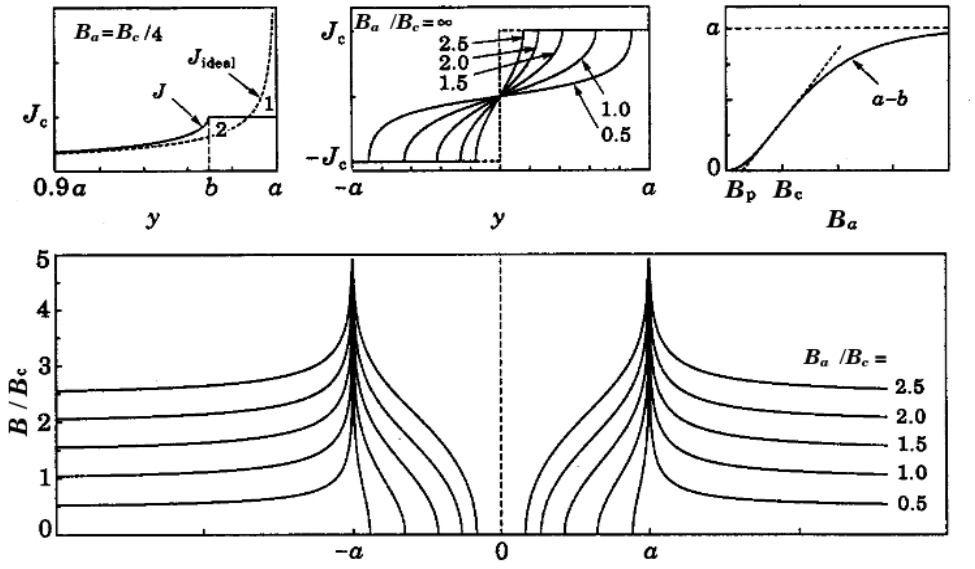

Figure 1.12: Topf kfl: saturation of the current density near the specimen edges at small applied field $B_a = B_c/4$. Top middle: current density J(y) in the strip for fields B_a/B_c = 0.5, 1, 1.5, 2, 2.5. Top right: penetration width a - b = a - a/cosh $(B_a/B_c)B$. Bottom. perpendicular local magnetic field B(y) for applied fields B_a/B_c = 0.5, 1, 1.5, 2, 2.5. Brandt et.al [26]

density.

The modulus of the current distribution vector field **J** will be constant[2], but because of the boundary conditions of the specimen it splits into domains of uniform parallel current flow [17]. The domains have different **J**-orientation and magnetic flux gradient direction, and are separated by discontinuity lines (d-lines) formed by sharp bends in the current density vector field (see figure 1.13), where there are no magnetic flux.

If the applied magnetic field is ramped up until we have d-lines as shown in figure 1.13b, and then decreased, the current at the edge will change direction and new discontinuity lines will appear between the center d-line and the edge. This is seen in figure 1.14 a) as bright lines and b) as two positive peaks.

[2]This is correct only for the simple critical state model, with the field independent critical currents

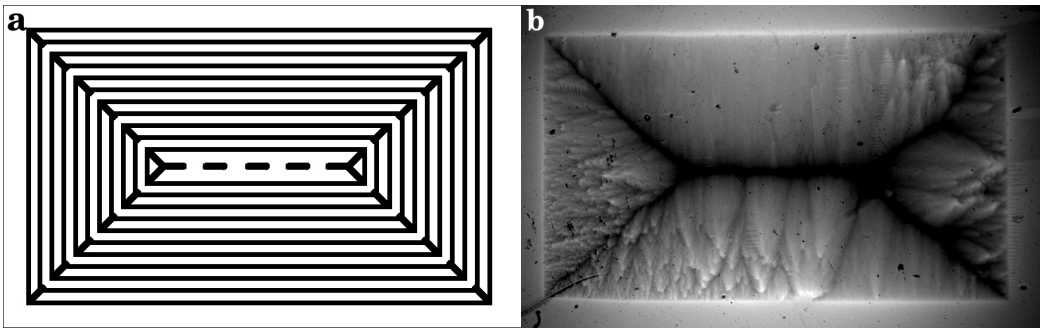

Figure 1.13: Current streamlines (left) and the normal component of the magnetic field in the critical state as a contour plot (right) in a thin type-II superconductor of rectangular shape, ref [27] and [17]

a

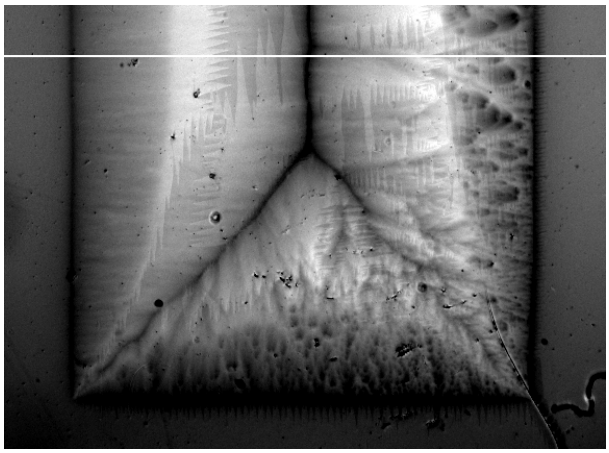

b

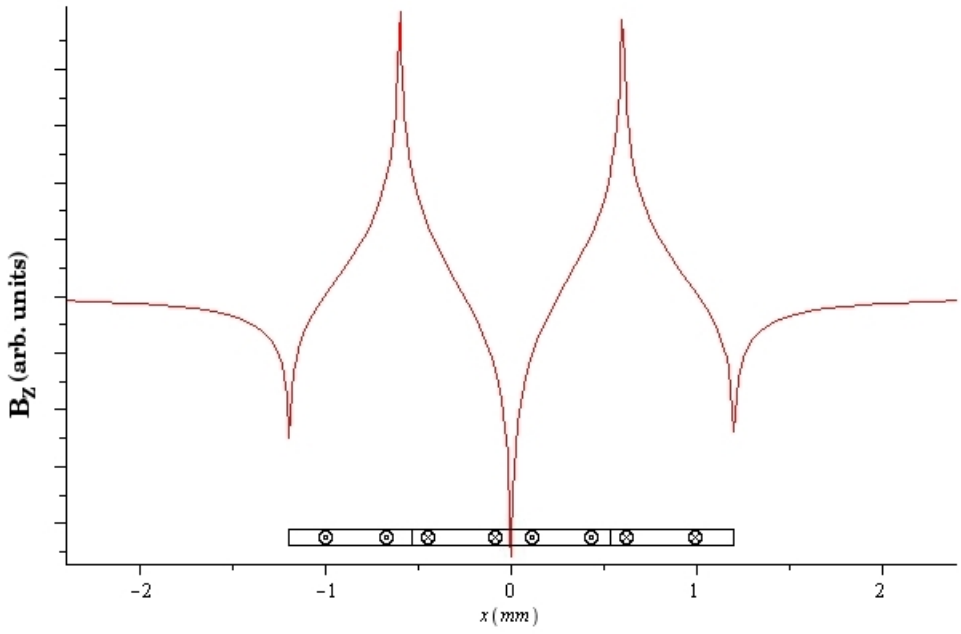

Figure 1.14: Profile of the magnetic field captured in a) magneto-optical image of NbN thin-film superconductor at T=10 K B_{app}=25.5 mT, b) numerically calculated by Maple for a cross-section of the short side of the (2.4 mm wide) sample. This is called a two-peak profile.

1.3 Thermo-magnetic instability

From the critical state model above (section 1.2) we know that if a magnetic field is applied slowly to a type II superconductor, new vortices will be produced at the edges of the specimen. The Lorentz force will move them toward the center, while the pinning force in structural irregularities will try to hold them back, forming a flux density gradient with a maximum at the edge of the superconductor and a minimum (no vortices) at a certain distance from the edge.

The critical state in these superconductors is not always stable, and can collapse due to thermally driven flux jumps resulting in a sudden large scale redistribution of vortices [28] [29]. These flux avalanches are due to thermo-magnetic instabilities caused by local heat-dissipation associated with vortex motion. This will reduce the pinning force and make it easier for more vortices to move into the sample. New vortex motion results in new heat dissipation, and we have a positive feedback. The avalanches may vary in size from only a few hundred vortices to millions spanning the whole sample (figure 3.11), depending on field strength and temperature [30].

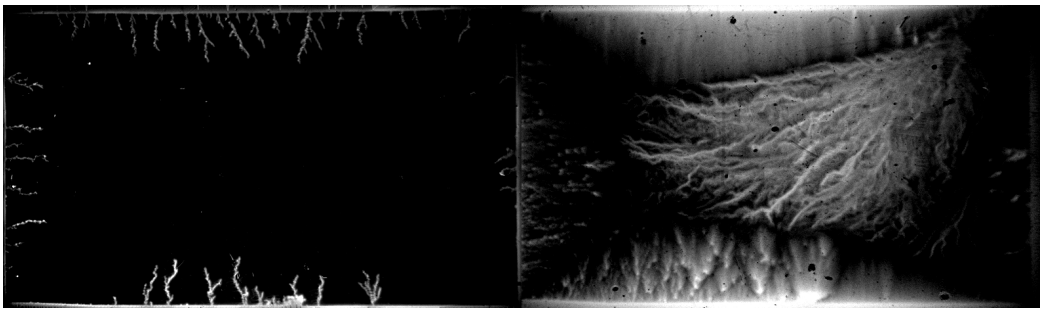

Figure 1.15: Size of thermally driven vortex avalanches. Left side; small dendrites at T=4 K and B=0.2 mT, right side ; large dendrites at T=7 K and B=43.5 mT

Avalanches also appear when the magnetic field is decreasing, with a dependence on temperature and field as mentioned above. But these are triggered by negative or reversed flux lines just outside of the sample, e.g. figure 1.16.

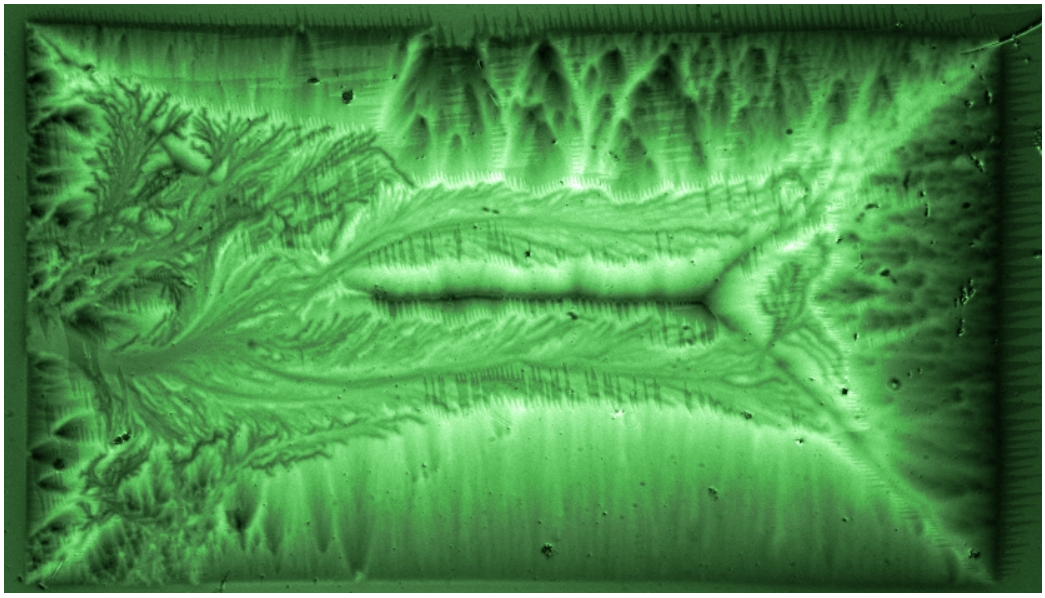

Figure 1.16: Thermally driven flux avalanches at decreasing fields in a thin-film NbN superconductor, at T=9 K and B_{app}=1.94 mT

1.4 Outline

The main goal of this thesis is to investigate thermo-magnetic instability in superconductor thin-films in as wide range of fields and temperatures as the experimental facilities permit. Magneto-optical imaging (MOI) is used to visualize the magnetic fields in the superconductor. The advantages of the MOI technique are non-invasive, fast reacting real time imaging, and the possibility of working on different length scales during an experiment. A phase-diagram of the thermo-magnetic instability in magnetic field (B) and temperature (T) coordinates will be constructed.

We will approach this goal by carrying out a set of automated real-time experiments on visualization of flux distribution and dynamics in the superconductor of choice. To analyze the massive graphical data, it is necessary to develop algorithms and routines for recognition of the dendritic patterns in MO images.

Given the goal and the available facilities, this thesis will concentrate on three main tasks:

- A program will be designed in LabView to control the digital camera

and the power supply, and to collect data from the experiments for later use.

- This program will be used to acquire images at different temperatures from 4K and up to where we have no more flux jumps, we know from previous works that this will occur above a certain threshold temperature [31] [29]. For every temperature chosen we will acquire images from zero field to above the upper threshold field where the flux jumps stop appearing, if permitted by the experimental facilities. The magnetic flux range will be down-sampled into sufficiently small intervals, such that the images acquired for every step will contain all important details of magnetic history of the sample, both with increasing and decreasing fields.

- In the end we will develop some routines in Matlab to extract the upper and lower magnetic field threshold values for all temperatures, and construct a phase diagram showing the magnetic field thresholds as a function of temperature.

Chapter 2

Experimental methods and setup

The magneto-optical imaging (MOI) method used in these experiments, is relatively user friendly, and the idea behind it is ingenious for it's simplicity. However, it has taken decades of research into the theories behind it to refine MOI to the prime technique it is today, and the results still rely on a high grade of accuracy and perseverance, and a little bit of luck.

In this chapter we will explain the method of magneto-optical imaging, describe the instrumentation used in the MOI setup, and give some information on the NbN thin-film superconductor sample used in these experiments.

2.1 Magneto-optical imaging (MOI)

There is a range of ways to visualize magnetic fields, like bitter decoration, different scanning techniques (MFM, SHPM, SSQUIDM), Lorentz microscopy, Hall probe array etc. While they are excellent for some tasks, like Lorentz microscopy for high resolution images of magnetic features on a scale of <10 nm, they do not have the same broad applicability range as the MOI technique. The most important advantages of MOI are i) it is non invasive, which means that the sample can be reused, ii) real time imaging, making it possible to observe the sample while changing the surrounding conditions and iii) the possibility of working on different length scales, even changing them during an experiment. Magneto-optical imaging has proven to be very applicable when investigating the magnetic properties of thin-film superconductors, and is now widely used .

The technique was first used in 1957 by P.B.Alers [32], who found it particularly useful when studying time-dependent phenomena. A drawback was it's limitations to high B_c superconductors. Even though minor progress was done, the big breakthrough came in the mid 1980's when it was found that iron garnet films, especially bismuth-substituted ones, with in-plane spontaneous magnetization [33] were excellent indicators. Now it was relatively easy (compared to how it used to be) to investigate the flux behavior in high temperature superconductors (HTS), and with some further development it was possible to visualize single flux-vortices in HTS [34], even in real time [16].

2.1.1 Faraday rotation

The technique is based on a phenomena called Faraday rotation (or Faraday effect), where the plane of polarization for a linearly polarized light is magnetically rotated in a dielectric medium with birefringence [35, page 101].

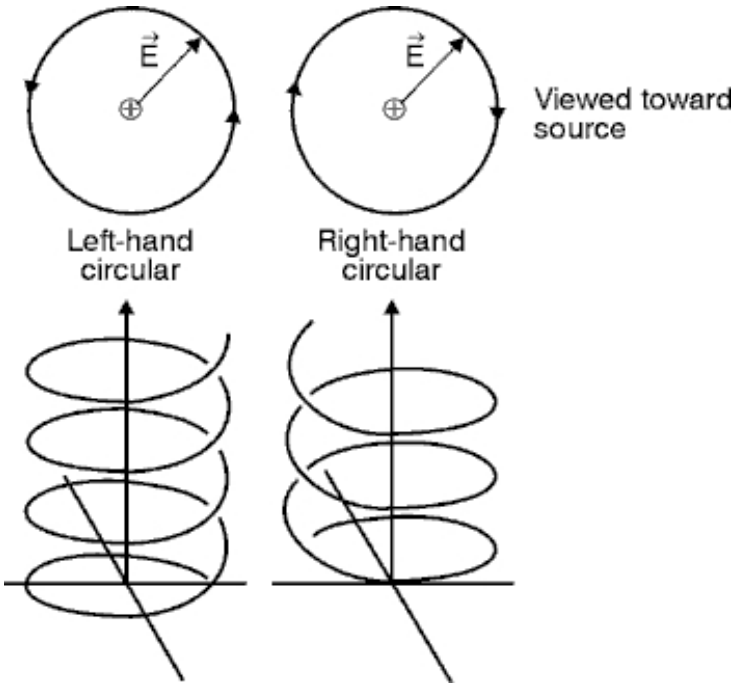

Figure 2.1: Two circularly polarized wave components rotating in opposite directions.

When linearly polarized light is sent into an anisotropic dielectric medium,

the permittivity will be represented by a second rank tensor, and we decompose the light into two circularly polarized components rotating in opposite directions (figure 2.1). If an external magnetic field (B) is imposed in the same direction as the incident light, it is seen that the two wave components have refraction indices that are not equal, leading to a difference in velocity between them when they propagate through the medium. When the two circularly polarized waves are recombined, now with a phase difference, into a linearly polarized representation, one sees that the phase difference gives a loss free rotation in a right-handed screw direction around B, with the (Faraday) rotation angle (θ) decided by the strength of B, the thickness of the medium (d) and the Verdet constant (V) (eqn. 2.1).

$$\theta = VBd \qquad (in \ \ radians) \tag{2.1}$$

The Verdet constant, which is not really a constant but a parameter, gives us the strength of the Faraday effect in a particular material. In addition to being material dependent, the Verdet "constant" is also frequency dependent.

2.1.2 The MOI-technique

High intensity light, in this case from a 100 W Mercury lamp, is sent through a polarization filter to give a linearly polarized light wave (see figure 2.2). This wave is reflected by a wave splitter and continues through the magneto-optical indicator film (MOI-film) where the Faraday rotation takes place.

It then reflects off the mirror layer (usually on the bottom side of the MOI-film, but sometimes the surface of the superconducting film is used) and returns back through the MO-film for double effect. The light then passes through the beam-splitter and is filtered by an analyzer, a polarization filter which is set at 90^o relative to the first one. Only light that is rotated will pass through the analyzer, stronger rotation gives higher intensity. In this way we can visualize the magnetic field passing through the MO-film.

2.1.3 Magneto-optical film

The anisotropic dielectric medium used to rotate the light in this setup is called a magneto-optical indicator film (MOI-film). There are many different compositions of this film, but the one that we use is the ferri-magnetic Bi:YIG film [33], a bismuth-substituted ferrite garnet sensor film (FGF) with in-plane spontaneous magnetization. A $5\mu m$ thick film is grown on a $Gd_3Ga_5O_{12}$

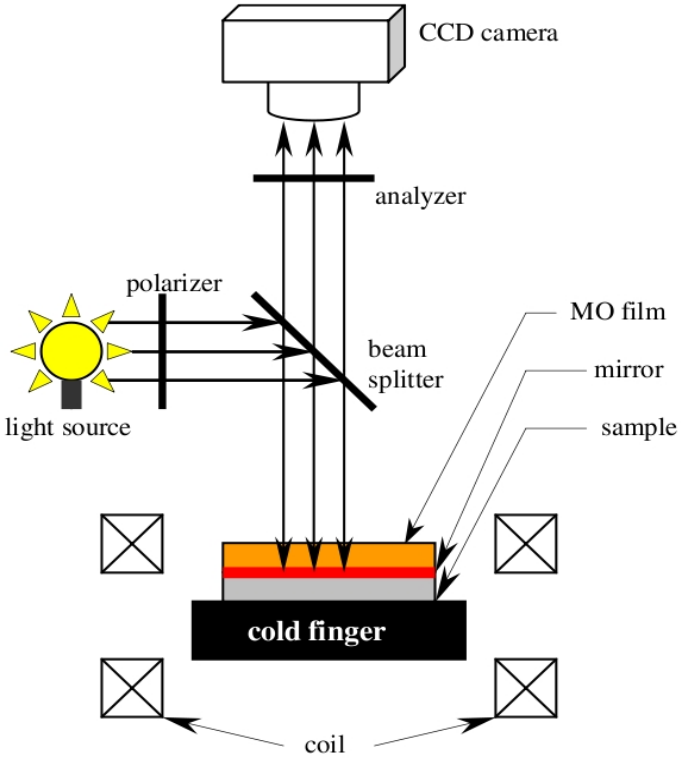

Figure 2.2: Schematic diagram of the magneto-optical imaging setup

(GGG) substrate, and then covered by an aluminium mirror layer, so that the light will be reflected back for double effect and detection by the camera.

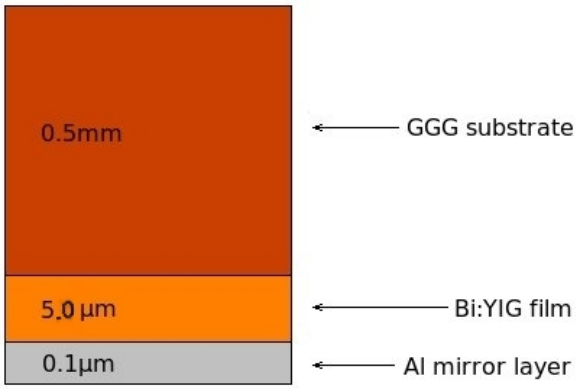

Figure 2.3: Cross section of a magneto-optical indicator film

2.2 Instrumentation

For some of the instruments in the experimental setup it might be beneficial to give a bit more information. This will give the reader some background to the possibilities and limitations of the setup.

2.2.1 Magneto-optical imaging setup

The sample is glued on to the sample holder of the cryostat with a little silicon vacuum grease. This vacuum grease secures a good conduction of heat between them when cooling down. On top of the sample we put a MOI-film. The sample holder is then carefully put into the cryostat chamber of the Oxford Microstat system, levelled and sealed. The Oxford Microstat continuous He-flow cryostat consists of a cryostat vacuum chamber with optical window, and a sample holder. An Oxford (GFS600) continuous flow transfer tube lowered into a liquid helium tank is cautiously inserted into the cryostat. Evaporated helium gas is pumped from the tank, via the transfer tube and through the sample holder with the aid of a He_2 pump (Oxford; GF3/VPZ0233). This cools down the sample, but to reach the needed temperature for the experiment ($4K$), we also need a high vacuum in the cryostat chamber ($\sim 10^{-7}$ mbar). A Pfeiffer (MVP 015T) high vacuum turbo pump mounted on the sample holder is used for this. With a cryostat of this design we are able to reach temperatures slightly below the boiling point of liquid helium, by keeping under-pressure in the transfer tube. To monitor the temperature we use an Oxford ITC-4 temperature controller, mounted to the sample holder.

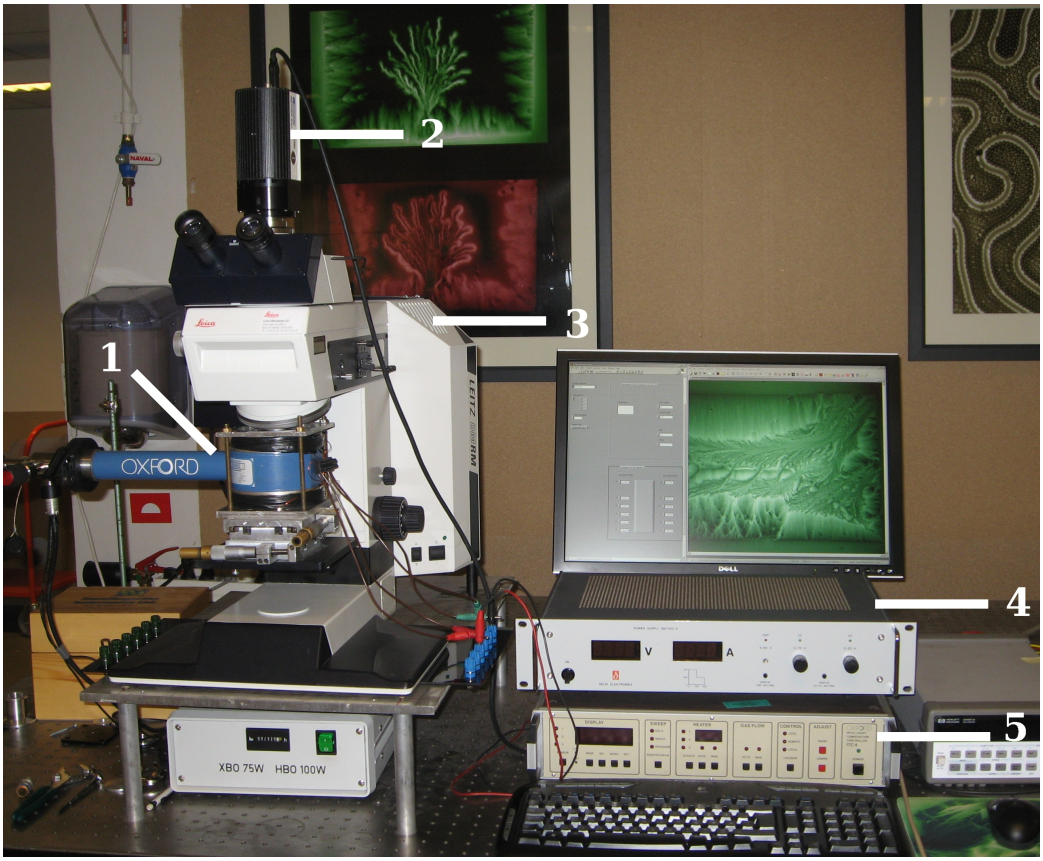

Figure 2.4: Magneto-optical imaging setup, consisting of; 1)Oxford continuous He-flow cryostat with resistive coils above and below, 2))QImagine 1.4 Mpixel CCD-camera, 3)Leica DMRM microscope, 4) Delta Elektronika power supply, 5)Oxford temperature controller.

In MOI we need to use a reflective light polarization microscope. This setup uses a Leica DMRM microscope, with Leitz eyepieces. A 100 W Mercury lamp (Leica HBO100W) is used to illuminate the sample. The cryostat chamber is mounted on an adjustable platform on the Leica microscope which can be adjusted in x-y-direction, in addition to z-direction, and the sample is observed by the microscope through the optical window of the cryostat.

Above and below the cryostat chamber we have resistive coils (see figure 2.2). These are connected to a Delta Elektronika power supply (SM7020D), with an output of ~10 A/70 V, and will induce magnetic fields through the

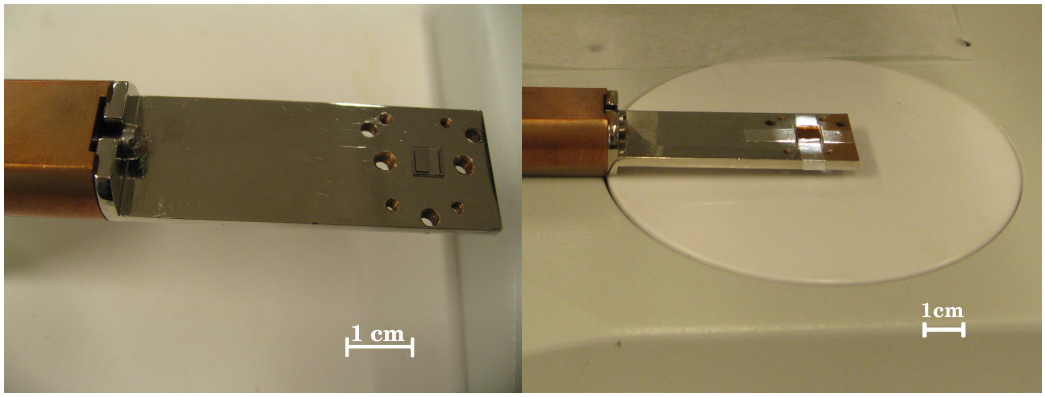

Figure 2.5: NbN-sample mounted on the sample holder (left), with a magneto-optical indicator film on top (right)

superconducting sample along the axis of the coils, strength of which is proportional to the current through the coils ($1A \Rightarrow 8.5mT$).

Images of the magnetic flux entering the sample are acquired with a QImagine Retiga EXi Fast1394 camera. This camera has a progressing-scan interline CCD (charge-coupled device) sensor, which gives a 12 bit digital output with a resolution of 1.4 Mpixel. The camera is connected via Fire-Wire^{TM} to a computer that controls the camera and stores the image data.

2.3 The samples

The samples we use in these experiments are superconducting thin films of Niobium Nitride (NbN), ~2000 Å thick. They were prepared by Senapati et.al.[36] on a single crystal (100) Magnesium Oxide (MgO) substrate by pulsed laser ablation of a high purity Nb target in a controlled ultrahigh purity (99.9996) N_2 environment. A KrF excimer laser (248 nm) operated at 20 Hz was used for ablation with pulse energy density of 5 J/cm^2 on the target surface. More detailed procedures and information on the structural characterization of the samples can be found in ref. [36].

2.4 Data acquisition by LabView

To control the QImagine camera and the power supply, and to collect data from the experiments we use the National Instruments LabView (Laboratory Virtual Instrumentation Engineering Workbench) 8.0 software package[1]. This is a platform and development environment that enables you to develop applications that perform scalable tests, measurements, and controlling of instruments.

The programs made with LabView are called "virtual instruments" (vi's), and consists of two interfaces; a front panel and a block diagram. The front panel is where you insert the initialization values, like minimum/maximum current, camera resolution etc., and observe events like images acquired by the camera. The block diagram is where you make the program, which is mainly to place pre-programmed vi's in a sequential way, give them the correct initialization parameters and wiring them together. LabView will to some degree required that you have experience in programming, but it is even more important to know the equipment used and the signalling between them and the computer where you run the software.

[1] http://www.ni.com/labview

Chapter 3

Results and discussion

As mentioned above, the thermo-magnetic instability exists only within a limited range of temperatures and applied magnetic fields. Determination of this range on the B-T phase-diagram is of an utmost importance for any potential application of superconductors. We will in this chapter focus mainly on construction of the instability phase diagram. At the same time a number of experimentally observed features will be discussed as they provide additional details important for understanding the flux dynamics in superconductors.

3.1 Distribution of the magnetic flux in NbN

In figure 3.1, a distributions of the magnetic flux in a NbN thin-film superconductor can be seen, representative for the temperature range within which the instability is observed. The images were recorded while ramping up the magnetic field after the sample was zero-field cooled to T=8 K. At small fields (figure 3.1 a), below the lower threshold field, only a shallow penetration is observed, with the flux front moving gradually inward with the increasing field. This smooth penetration ended abruptly when reaching B=2.72 mT, where a flux avalanche suddenly appeared. The avalanche area is seen in figure 3.1b), and we see the branching structure rooted on the lower sample edge. As we further increased the applied field, more and more avalanches took place, creating a complex pattern of flux dendrites covering most of the sample area (see figure 3.1c at B=7.23 mT). Then, as the field reached B=8.67 mT (figure 3.1d), the avalanche activity stopped completely even though we continued to increase the magnetic field. The advancing flux front now erased the previously formed dendritic structures (figure 3.1e), and

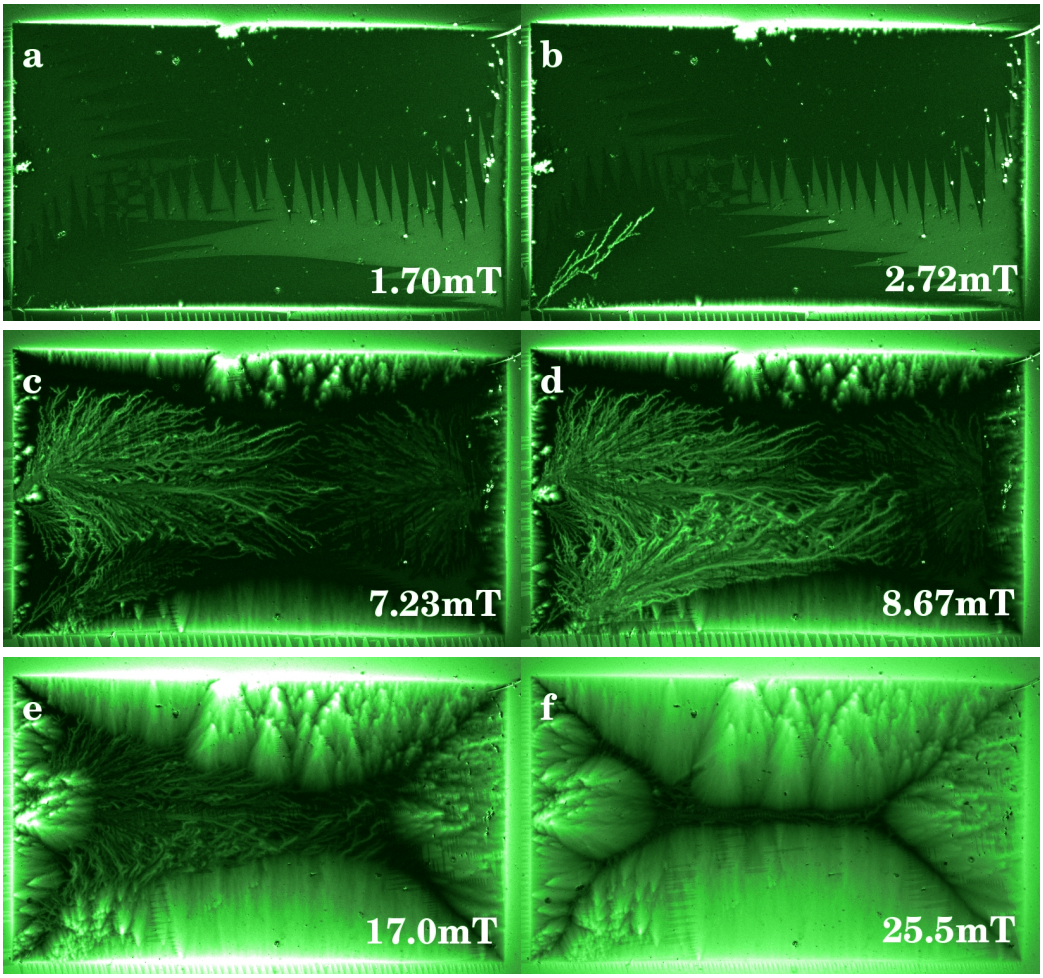

Figure 3.1: Magneto-optical images of a NbN thin-film superconductor at T=8 K where the applied field is increased. The film is 4.8 mm long and 2.4 mm wide.

the critical-state mode of flux penetration was restored (figure 3.1f).

The moment when the dendrites start forming in a superconductor can be easily recognized in real time experiments by looking in the microscope, or from the magneto-optical images. However, in many cases when conducting constructive analysis of the phenomenon it is desirable to track the history of the flux front, starting from just before until shortly after an avalanche takes place. When acquiring the images manually, an operator must simul-

taneously take images, run a log of experimental conditions, and adjust their values (e.g. field, temperature). Besides being a very tedious and time consuming process, it very often leads to a loss of data. For example, in order to take a series of images at increasing field one has to be able to take an image, write down the values of the different variable parameters like exposure time, current field and temperature, and save the corresponding picture on a hard drive. Further increase of field results in increasing intensity of the light projected on the CCD matrix of the camera, which often causes over-exposure and consequently a loss of visual information if not calibrated. And when processing the images manually afterward, it is not always easy to distinct new incidents from old (e.g. figure 3.5).

3.2 Automation of the experimental setup

In order to make the acquisition of data more convenient and loss free, and the subsequent analysis more complete, a corresponding automation procedure must be developed. Taking into account the diversity of experiments carried out in the superconductor laboratory, it seems to be rather unrealistic to create a unified program that would suit all types of samples and measurements. However, based upon the experience collected by me and other members of the group, it is possible to select a number of generic features that have to be included specifically for investigation of thermo-magnetic instability.

Communication between a computer and instruments in the experimental setup can be carried out through a number of programs and programming packages. For practical reasons the preference has been given to LabView. A LabView program, "CEFA4.vi" was developed to control how the power supply provides current to the resistive coils, and to control the CCD camera. The output of the power supply should be accurate enough to ensure a reliable control of the magnetic field induced by the magnetic coils. The current should also be changeable in predetermined steps, the value of which is to be set in the front panel interface, in addition to the maximum current. Accuracy of the B-field is constricted by the power supply accuracy, since this is not as good as on the output card. According to the data sheet of the SM7020-D power supply[1], the programming input has an accuracy of 8mV. This gives, with a resistance of $R \sim 5\ \Omega$ in the coils, an accuracy of $\Delta I = 1.6\ mA$, or with the translation factor $8.5\ \frac{mT}{A}$ a $\Delta B = 13{,}6\ \mu T$.

For every ΔB we want the camera to take an image, change the exposure time and take another image. This is for comparing two consecutive images, where the only variable changing is the applied magnetic field, which enables us to accurately determine how the superconductor is influenced by this change. It is also important to change the exposure time along with the B-field, to ensure that the images don't get over exposed at high fields and loose information. The images will be stored in a predetermined place, and we also store information on B-field and exposure time for all images, see table 3.2.

There are different ways of automatically adjusting the exposure time (t_{ex}) while running the experiment: One can decide on a maximum intensity al-

[1] http://www.delta-elektronika.nl/PDF/DTS-SM700.pdf

lowed in the image, read out the highest intensity of any pixel in the image and adjust t_{ex} accordingly. Alternatively one can read out the average intensity of the image and adjust t_{ex} so that you end up with an ideal, predetermined average intensity. The first method is relatively fast, which is important for this setup to limit the heating of the resistive coils. We want to send currents of up to 10A through them, and if they become too hot the current/voltage limit of the power supply will prevent us from reaching these high currents. The problem with this method is that defects in the sample or MOI-film might give some bright spots that is not representative for the image intensity, and can render the image too dark.

This is not a problem with the second method, where the bright spots will be averaged out. On the other hand, this method is slow compared to the first, and will render the resistive coils too hot. Both of these methods require that you go through the current range manually in advance, and look at what the parameters gain and offset, need to be. When acquiring the images from the camera, the analogue image data is multiplied by a gain and added to an offset, so it will better fit the digital scale before it is converted into digital numbers. If there is certain aspects of the sample/image that is desirable to enhance, one can use gain and offset for this.

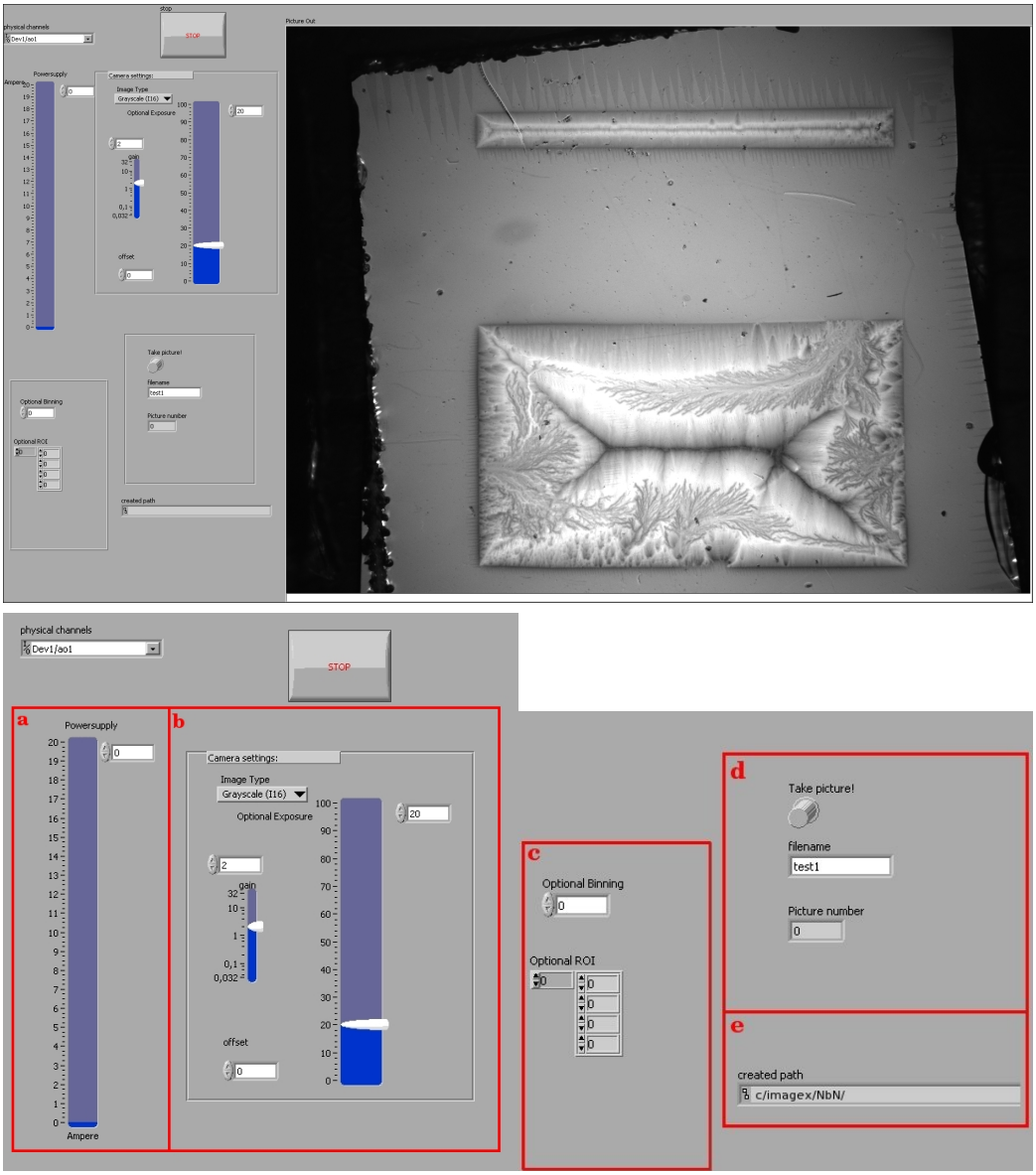

Figure 3.2: Top: Front panel of Imagecontrol.vi. Bottom: Enlargement of the Imagecontrol.vi control panel. In addition to the choice of physical channel and the stop button, we have a) current control, values entered by dragging slider or typing in directly, b) control of the camera parameters; gray-scale, gain (slider or typing), offset (typing) and exposure time (slider or typing), c)additional camera parameters; region of interest (ROI) and binning, d) button for acquiring images, field for typing in a name for the image that will be merged with the picture number shown in window below (in this case to: 0test1.tif), and e) a window showing the path to the folder where data are stored

The third method, and the one we use is to find an algorithm for the coherence between the current and the intensity in advance, and let LabView (CEFA4.vi) calculate a new t_{ex} for every current step. In addition to finding suitable values for gain and offset, we also look at what t_{ex} gives ideal intensity in the image at different values of the current (I), choosing I=0.1, 0.3, 0.5, 0.7, 1, 1.5, 2, 2.5, 3, 4, 5, 6, 7, 8, 9, 10 A and back down again since t_{ex} will be different on return (decreasing B-field). We developed a program called Imagecontrol.vi (front panel: see figure 3.2, block diagram: see appendix figure A.5) to help us extract this data. All important parameters on the camera can be adjusted in real-time together with the current output from the power supply, simplifying the collection of the data. The values of I

Current (A)	Optimal exposure (ms) increasing fields	Optimal exposure (ms) decreasing fields
0,1	15	11
0.3	10	8
0.5	7	5
0.7	5.5	4.5
1.0	4.3	3.4
1.3	3.2	2.4
1.6	2.3	1.9
2.0	1.7	1.4
2.5	1.4	1.1
3.0	1.1	0.87
3.5	0.88	0.71
4.0	0.72	0.60
5.0	0.53	0.46
6.0	0.43	0.36
7.0	0.34	0.32
8.0	0.29	0.29
9.0	0.26	0.26
10.0	0.24	0.24

Table 3.1: Ideal values for exposure time t_{ex} for different applied fields (expressed in applied current values) at T=4 K, with gain=3 and offset=400. These were fitted in Origin with the equation 3.1, and illustrated in 3.3

and T_{ex} are fed into a program called "Origin"[2], a scientific graphing and data analysis software package, where an exponential fitting to this algorithm is

[2]http://www.originlab.com

done:

$$Y = Y_0 + A_1 e^{-\frac{(x-x_0)}{t_1}} + A_2 e^{-\frac{(x-x_0)}{t_2}} \tag{3.1}$$

where Y=t_{ex}, x=I, and the rest are fitting parameters calculated by Origin.

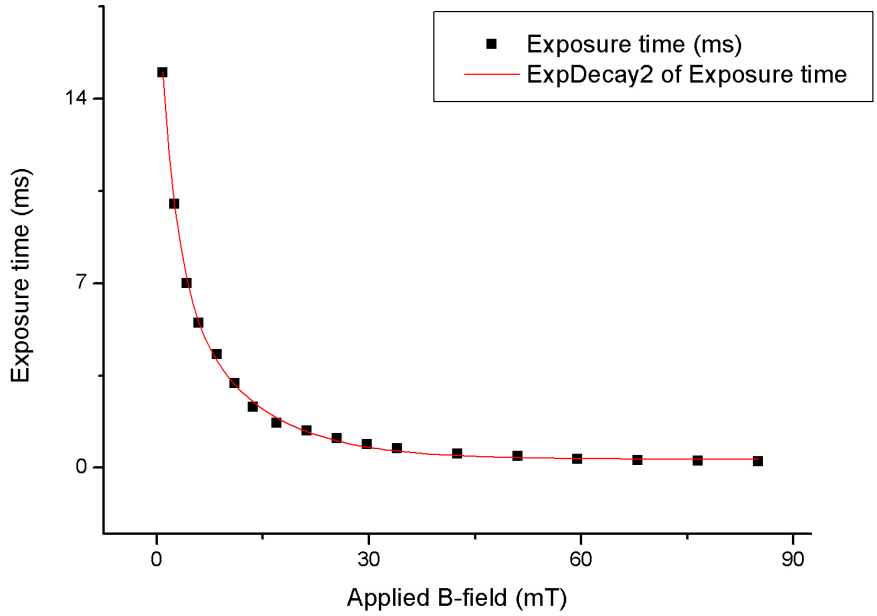

Figure 3.3: Exposure time t_{ex} at different applied magnetic fields B_{app}, and the fitting curve for the coherence between the field and exposure time

An illustration of the fitting curve can be found in figure 3.3. The algorithm is integrated into the LabView program CEFA4.vi, and the parameter values are entered in the front panel.

3.2.1 CEFA4.vi

If we look at the front panel first (see figure 3.4), the program interface is user friendly, and can be operated by anyone with a quick look through this thesis.

The block diagram can be divided into three parts; initialization, operation and termination, see Appendix A figures A.2, A.3 and A.4.

Figure 3.4: Front panel of CEFA4.vi, with a) physical channel selection for the power supply, and additional camera parameters; region of interest (ROI), binning and gray-scale, b) the parameters for the experiment, which is temperature (not controlled via LabView, but concatenated into the directory name for data storage), max current, current steps, gain and offset, c) parameters used in the algorithm for calculating the exposure time, we need different sets of parameters for increasing and decreasing B-field

In the first part we open up connections to the camera and the power supply, and initialize these with the variable initialization parameters set in the front panel, and static values from the camera software. Initial t_{ex} is also calculated here from the values set in the front panel. This is also where we set the path to where we want to store the files.

Most of the processes of the second part are executed repeatedly in a for-loop, which runs until the power supply has reached it's maximum current I_{max} at steps of ΔI, and decreased to zero again: $(n = 2 \cdot \frac{I_{max}}{\Delta I} + 1)$. The loop is divided into four parts. The first is where we change the current value, and calculate the exposure time. As mentioned above, the parameters are different for increasing and decreasing B-field, so we need to use a case structure with two sub-diagrams (see Appendix A figure A.1). Which one will be executed depends on whether the B-field is increasing or decreasing. The current is immediately adjusted, but t_{ex} is not changed before the fourth part of the

loop. As mentioned above we need two images at every step for the analysis to be satisfactory; one after we change the B-field but before we adjust t_{ex}, and one after the adjustment of the exposure time. The second part of the loop is just a time delay of 40 ms, to give the power supply time to adjust, and sample time to react, before the first image is acquired in the third part of the loop. In the fourth part t_{ex} is changed, and another image is acquired. We also store the current and t_{ex} with the name of this second image in a data file (named "data.dat").

Image file name	Current (A)	Exposure (ms)
0.tif	0.000	20.059
1.tif	0.025	18.586
2.tif	0.050	17.253
3.tif	0.075	16.048
4.tif	0.100	14.958
5.tif	0.125	13.971
6.tif	0.150	13.077
7.tif	0.175	12.266
8.tif	0.200	11.531
9.tif	0.225	10.864
10.tif	0.250	10.258

Table 3.2: Example of data stored in a data.dat file, here is data for the first images at T=4 K

When we have captured all the images that we need, and stored all the data, we stop the camera and close the connection, clear all tasks for the power supply and close the data file, before terminating the program.

3.2.2 Algorithm for graphical recognition of magnetic flux avalanches

When we want to analyze the data collected by LabView by comparing images or process them in some way, we use the numerical computer environment Matlab, since it allows for easy matrix manipulation, and has a rather basic script language. MO images are stored in TIFF format, which can be converted by Matlab built-in functions into a 2D array of gray levels that, in turn, can be converted into the field values. The images acquired by the camera are 12 bit gray-scale, but saved in the computer as 16 bit. The colored images are processed later for better visualization of the shade of difference.

First we isolate the new dendrites when they emerge by subtracting two adjacent images with the same exposure time. Then we filter out noise and convert the images from 16 bit to 8 bit. In figure 3.5a and b, the reader can see the two adjacent images, separated in B-field by only $213\ \mu T$. The difference image 3.5c shows the dendritic pattern that arise from this increase in the magnetic field. The Matlab-program made for this task is "difference.m", which you can find with comments in appendix B.1

Second we develop another algorithm that search through the difference images to find at which applied field we have these dendritic avalanches. For this task we made the Matlab program "finddend.m", see appendix B.2. The difference image was divided into squares of $\Delta B = 23 \times 23$ pixels, see figure 3.6, and in each square we calculated if the intensity was higher than a certain value. This value, which is a sort of high-pass noise filter, is calculated in Matlab with an algorithm fitted by the program Origin (eqn.3.1). If the intensity is high enough (giving white fields in figure 3.6) in at least two adjacent squares, we presume that we have a dendritic avalanche. It is crucial that the noise filter values used in this program are set carefully, or we might end up seeing noise as flux jumps, or not seeing anything at all. We then record the field values corresponding to the first and the last images where dendritic patterns are found, both at increasing and decreasing magnetic field.

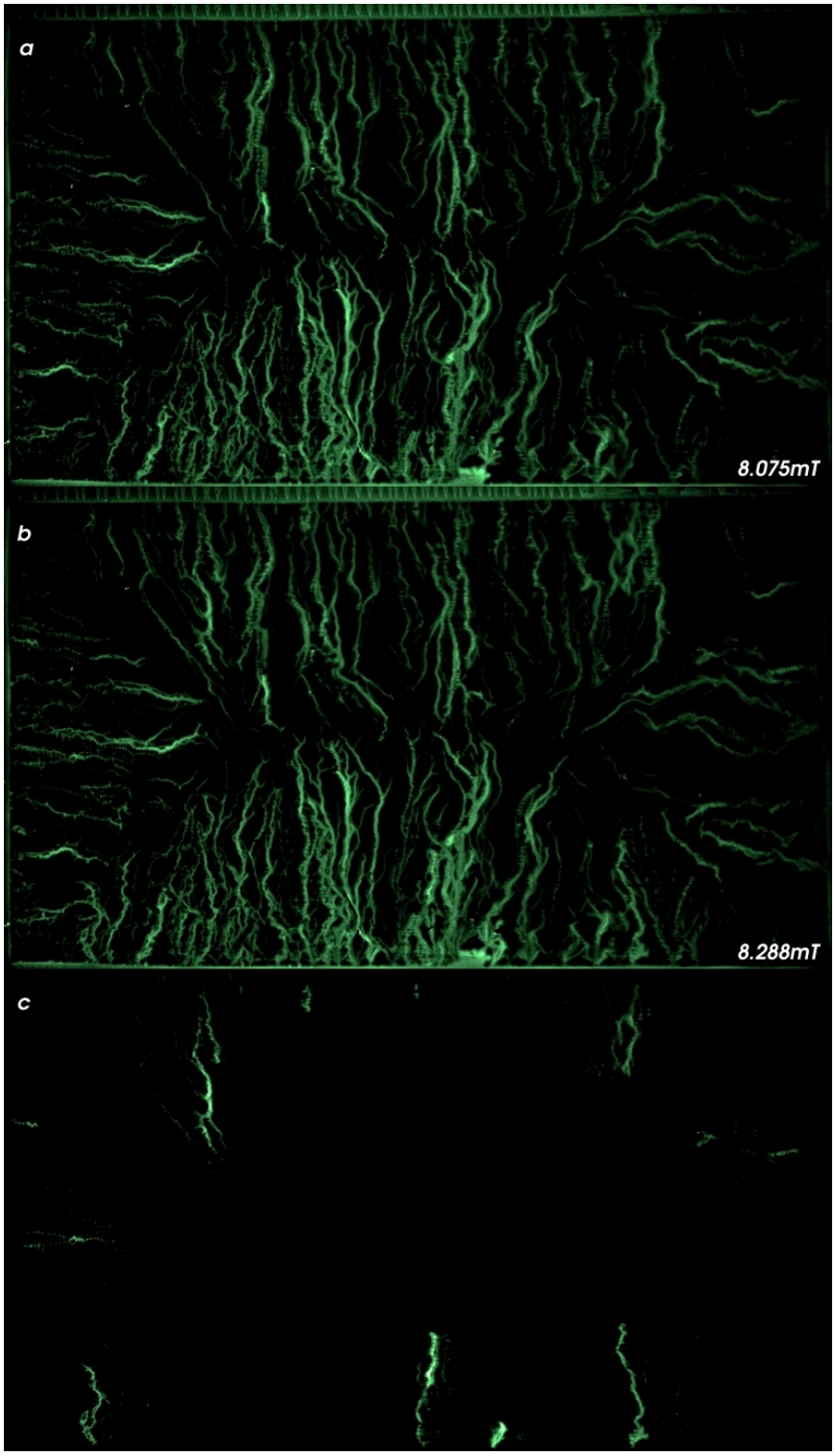

Figure 3.5: Subtraction of two images at T=5 K, the bottom image is a difference image of the two above.

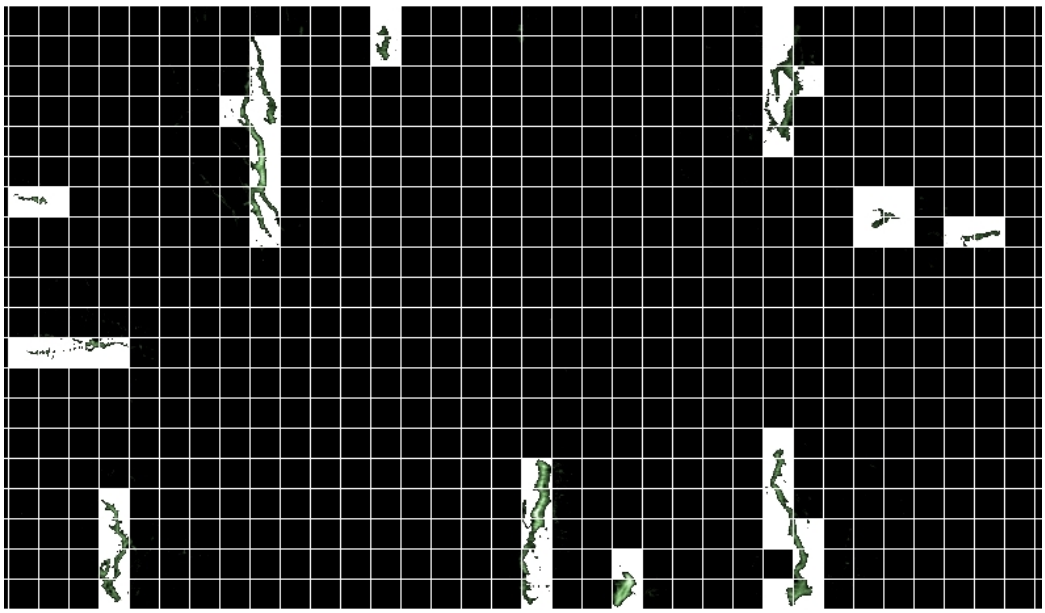

Figure 3.6: Difference image in figure 3.5, with a grid. White areas indicates that the intensity is high enough according to a predetermined threshold value.

3.3 Phase diagram

The experimental procedures and analysis as described in 3.2 were carried out in a range of temperatures from T=4 K to T=10 K with an interval of ΔT=1 K. Two additional measurements were taken at T=8.5 and T=9.5 K. The resulting phase diagram is presented in Figure 3.7. The upper threshold

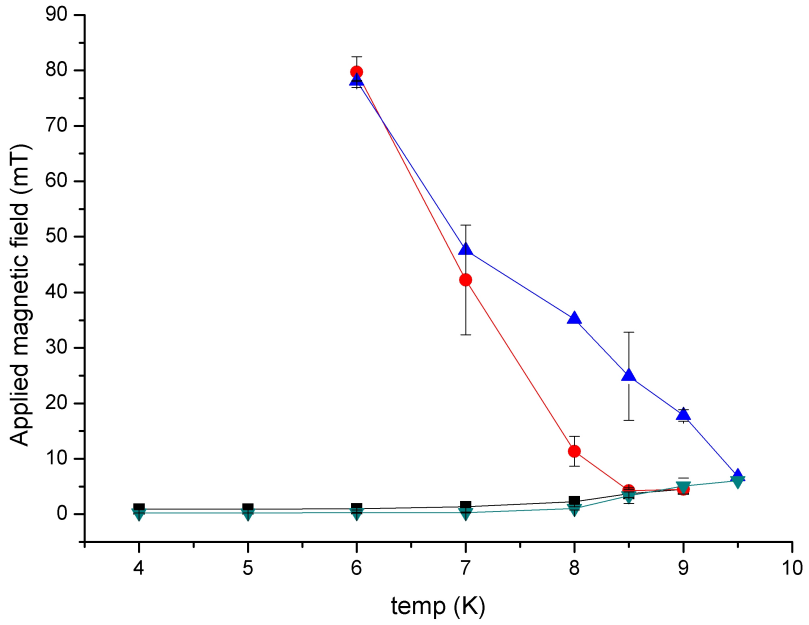

Figure 3.7: Phase diagram showing the thermo-magnetic instability thresholds for increasing and decreasing fields, as a function of temperature. Square and circle indicates thresholds at increasing fields, triangle and inverse triangle indicate thresholds at decreasing fields.

fields at T=4 K and T=5 K was not measured since this MOI setup could not generate a perpendicular field above B=85 mT. Rudnev et.al [37] have found the upper threshold for increasing fields at T=4.2 K to be $B \approx$100 mT.

An interesting observation is that between T=7 K and T=9.5 K the upper thresholds for increasing and decreasing fields separate, with the threshold for decreasing field being substantially higher, while the lower threshold fields seem to coincide within the experimental error. Such a hysteretic behavior has previously been observed experimentally, but an explanation of

the hysteresis was missing. Yurchenko et.al [29] explained the disappearance of dendritic avalanches within the framework of the theoretical model developed at the superconductivity group and presented in a series of publications: [38] [39]. Re-entrant thermo-magnetic stability of superconductors was interpreted in terms of the field dependence of the critical current [29]. Figure 3.8 schematically shows a correlation between the threshold field and j_c.

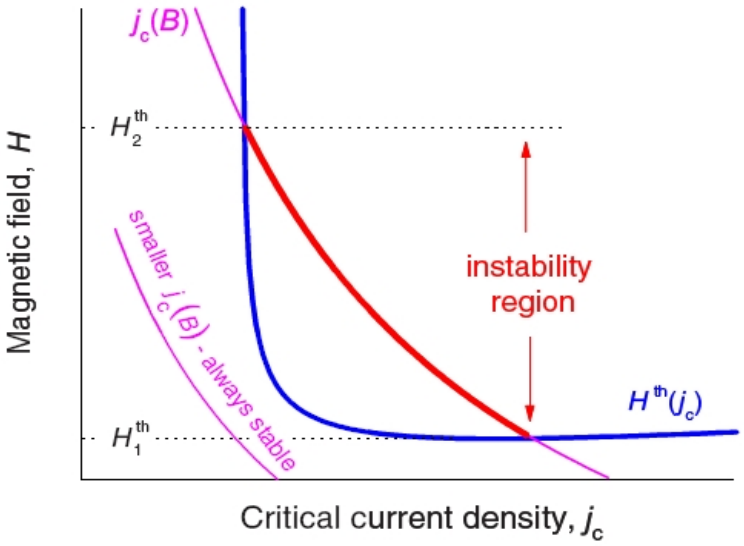

Figure 3.8: Schematic plot illustrating the existence of two threshold fields for the dendritic instability. The two main curves represent the threshold field H^{th} versus j_c and a typical monotonous field dependence of the critical current density ($H^{th} = B^{th}/\mu_0$). The intersection of the two curves defines the two thresholds H_1^{th} and H_2^{th} for the onset and vanishing of the instability, ref [29]

At small critical currents the threshold field diverges, which means that this field can not be reached, and no avalanches appear. However, if the critical current is strong enough, we will at some applied magnetic field reach the lower threshold field, making the superconductor thermo-magnetically unstable. But the critical current density will decay with the applied field, meaning that when the field is increased, there will be a point where current becomes so small that the corresponding threshold field is unattainable, i.e. the superconductor will be thermo-magnetically stable again. In order to understand the hysteresis on the phase diagram one has to consider the magnetic field profiles in the superconductor as it is schematically shown in

figure 3.9. This is obtained as a direct result of integration according to Biot-Savart's low.

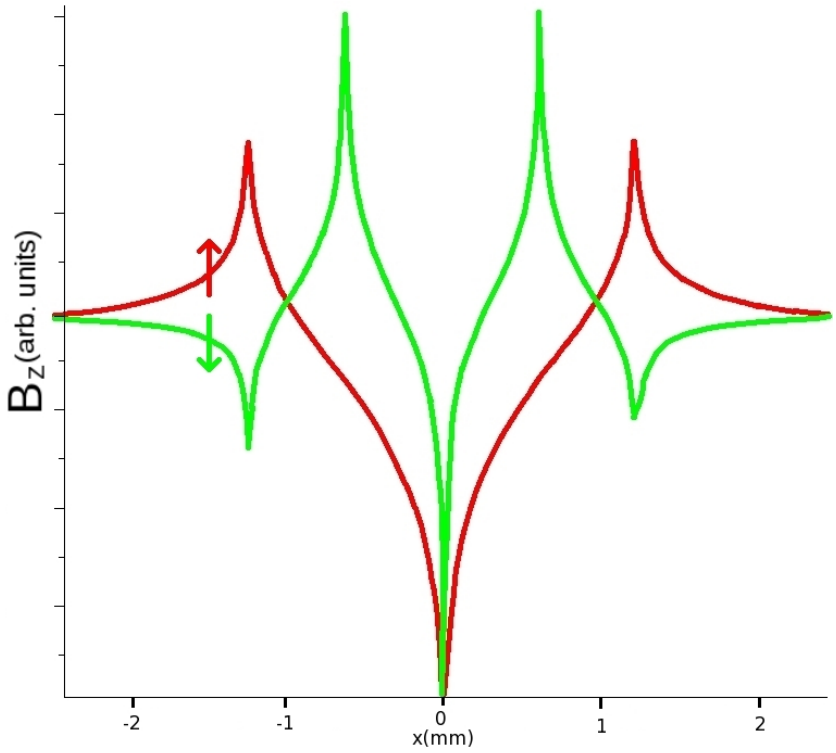

Figure 3.9: Profile of the magnetic field across the short side of a 2.4 mm wide sample, at increasing (red) and decreasing (green) magnetic field, numerically calculated by the Biot-Savart law.

When the applied magnetic field is increased, a build-up of magnetic flux just outside of the film can be observed. Local value of the field inside the superconductor depends on the critical current, which is a function of temperature and field [$J_c = J_c(|B|, T)$], and is therefore a result of a self-consistent solution. Since the avalanches originate from the edges of the sample, the important parameter will be the local field close to the edge. The dendrites will be formed until the field reaches the upper threshold (red curve in figure 3.9), but the flux will continue to penetrate further into the sample until it fills up the entire volume according to the critical state model. When the field after reaching some maximum is decreased, the currents flowing close to the edge will reverse their direction, leading to deep minima in the field profile on the edges. This means that at the same applied field, the induction on the edge

of the superconductor may differ substantially, depending on the magnetic history. The values of the critical currents will change correspondingly; and the absolute value of the critical current will be higher on the descending branch because of the field-compensation effect.

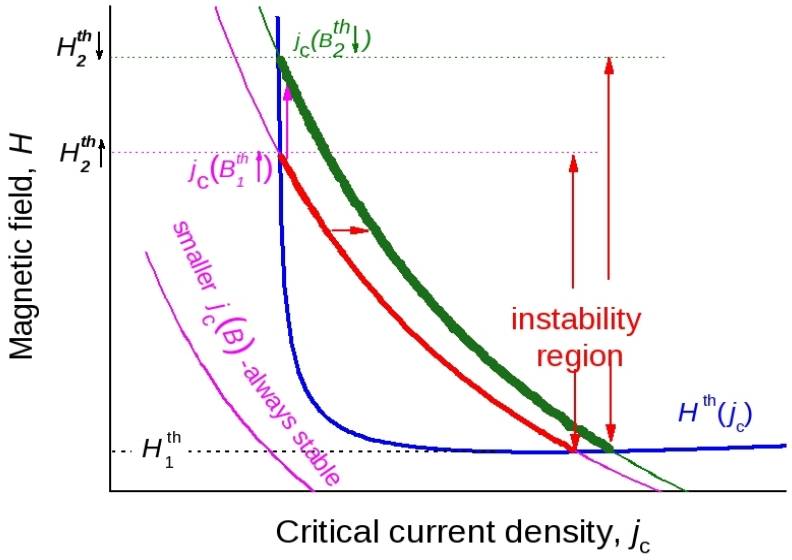

Figure 3.10: Schematic plot illustrating the dendritic instability thresholds for both increasing (red) and decreasing (green) fields

The $j_c(B)$ line that defines the instability region becomes effectively shifted towards the higher critical currents, which results in an increase of the threshold field (figure 3.10). In this particular sort of samples, for intermediate $j_c(B)$ the threshold field changes very little with the current, therefore the lower threshold fields stay practically unchanged for increasing and decreasing fields. Interestingly, the hysteresis on the phase diagram disappears at temperatures below T=6.5-7 K. This is due to the fact that at lower temperatures the critical currents increase and so do the fields induced by them on the edge of the superconductor. At a certain temperature (in our case at around T=7 K) the local field minimum will become negative and its absolute value will be comparable with the one corresponding to the upper threshold field on the increasing branch. Eventually, the local values of the critical currents will be very similar and a difference in the threshold fields negligible.

3.4 Flux dynamics

The thermo-magnetic instability makes the flux dynamics in NbN thin-film superconductors very rich on effects. While studying the limiting mechanisms of the flux avalanches, we observed a number of well established as well as new features.

3.4.1 Size of flux jumps

It has been established experimentally that flux jumps due to thermo-magnetic instabilities will increase in size with increasing magnetic field for thin-film and slab superconductors of various materials [30]. Figure 3.11a,b shows flux

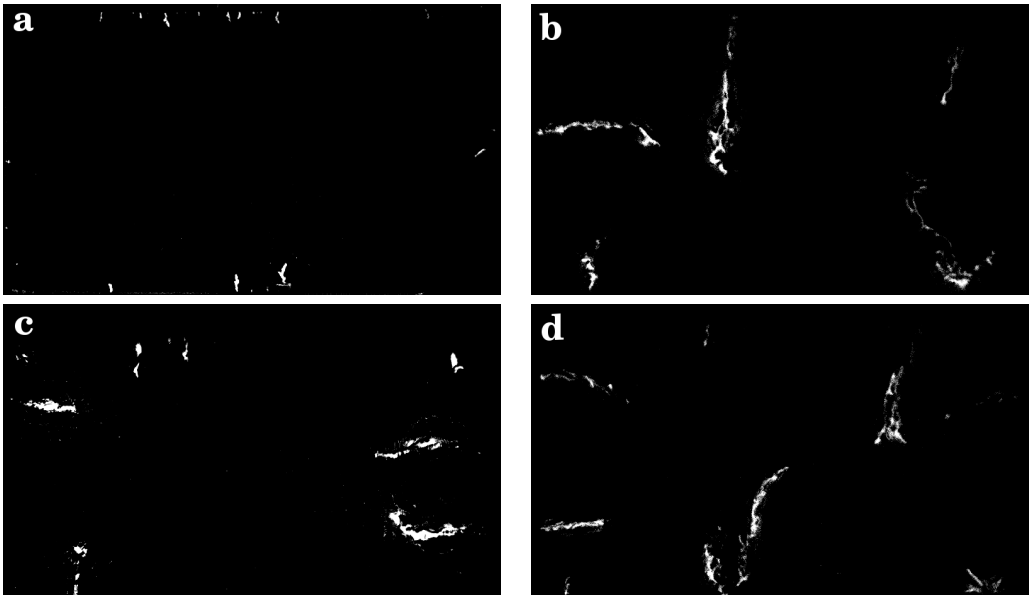

Figure 3.11: The difference images showing the size of flux jumps for 2.55 mT (left) and 79.16 mT (right), a and b are increasing fields while c and d are decreasing fields

jumps at increasing magnetic fields for B=2.55 mT and B=66.73 mT respectively, and 3.11c,d do the same for decreasing fields. We also see that the flux jumps get a more complex pattern at higher applied fields. One reason for the increasing size and complexity of the flux jumps is a higher density of vortices throughout the specimen. The heat originating from the motion of a vortex will therefore to a greater extent interact with other vortices before

it dissipates into the surrounding environment, resulting in more vortices being de-pinned and relocated. Notice also that the difference in size is not as evident for decreasing magnetic fields as they are for increasing fields. Phase diagrams have been elaborated for the cohesion between the size of flux jumps and magnetic fields [40] [30]. They show also that the number of flux avalanches decrease as the size of the avalanches increases. We observe that the results are also applicable for these experiments.

A similar trend is observed for increasing temperature (figure 3.12). Temperature also affects the shape of the avalanches, giving a noticeable increase in fractal dimensionality as field and temperature increases.

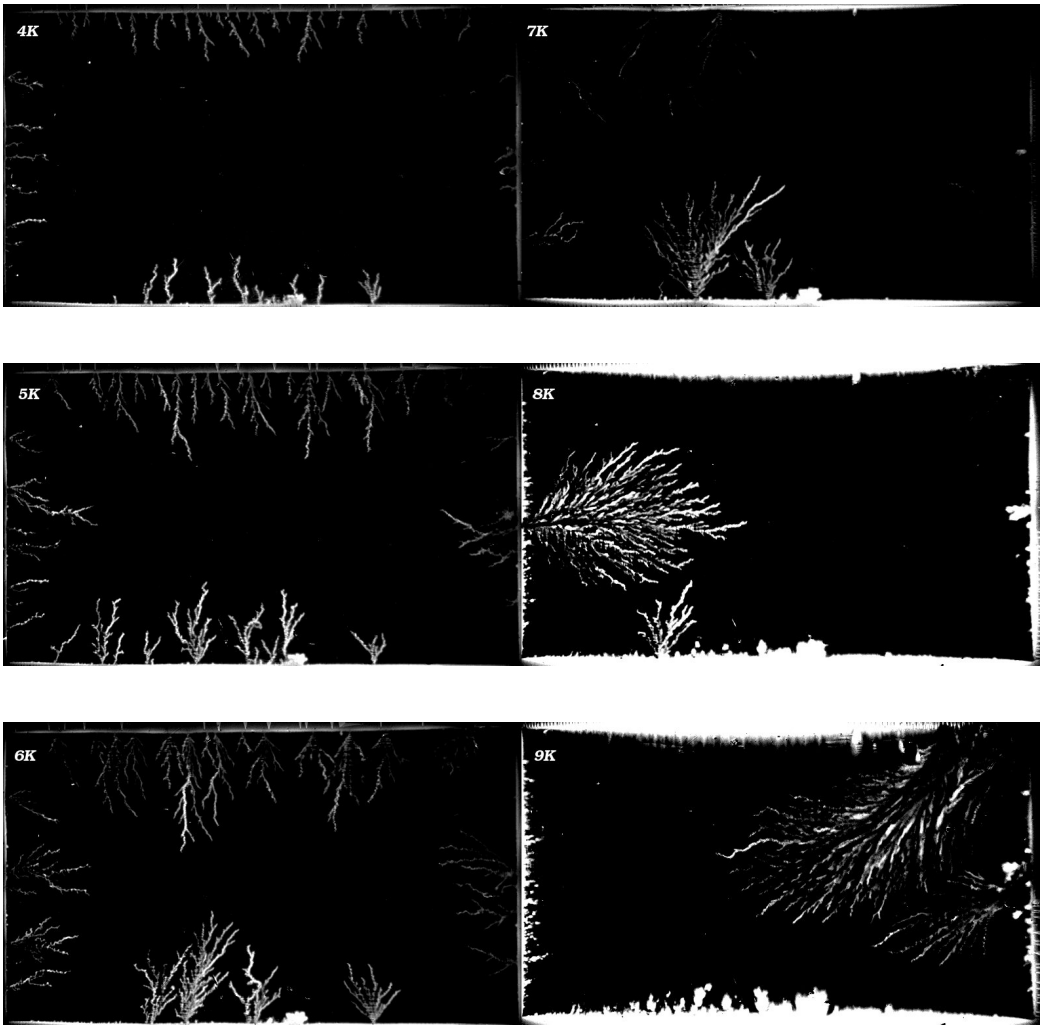

Figure 3.12: Difference images of flux jump patterns at T=4 K, 5 K, 6 K, 7 K, 8 K and 9 K for increasing fields, at B=1.70 mT, 2.13 mT 2.55 mT, 2.68 mT, 3.40 mT, 4.50 mT respectively

3.4.2 Large flux avalanches

At temperatures from T=7 K and above we have several large avalanches filling most of the superconductor, which may seem strange if one bears in mind the Lorentz force due to the shielding current circulating in the film (figure 3.13). This force drives the vortices and predetermines a direction

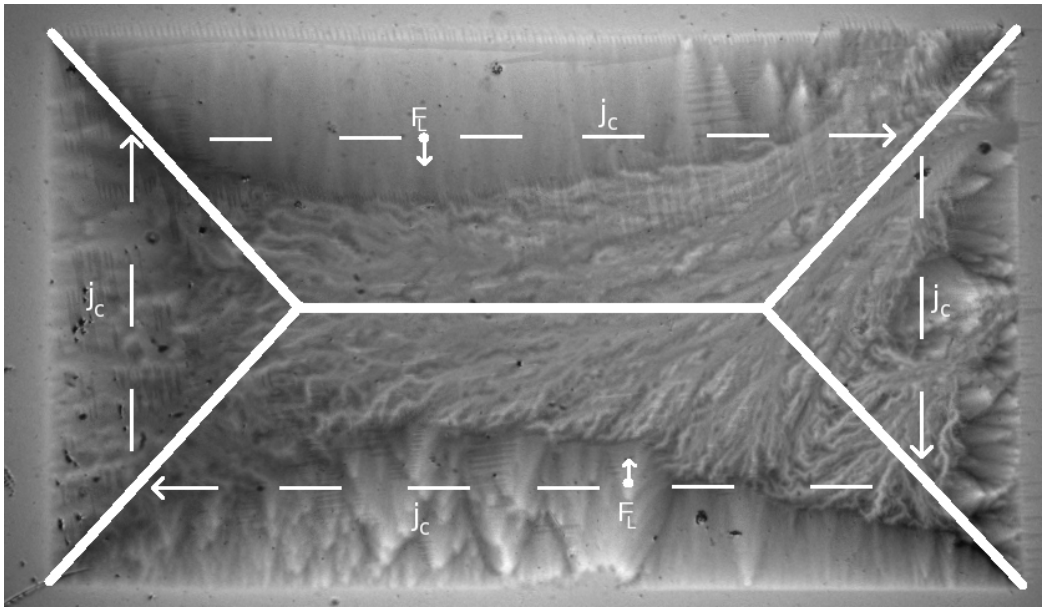

Figure 3.13: Magneto-optical image of NbN thin-film superconductor at T=7 K and B=26.4 mT. We see the d-line plotted with the corresponding directions of the critical current and Lorentz force. The avalanche has propagated autonomously of the direction of the critical current, and have filled the area inside of the flux front.

of the avalanche propagation. Since vortices have no inertia, one would presume that they would not cross over the central d-line of the superconductor.

A possible explanation to this puzzling effect is that at high temperatures these huge avalanches produce enough heat to totally suppress superconductivity in their massive cores. This and the collapse of the critical state in a large part of the sample will divert the shielding currents to flow according to the new electro-magnetical landscape, and the Lorentz force drives the avalanches to fill the area with low density of vortices, which is the area inside of the regular flux penetration front.

If the applied field is sufficiently above the magnetic instability upper threshold field, a central d-line will form as the vortices penetrate the superconductor according to the critical state model. If we then start decreasing the applied magnetic field upon reaching a certain maximum, a new discontinuity line is formed in between the d-line in the center and the edge of the superconductor (figure 3.14a and c). As can be seen in figure 1.14, we have

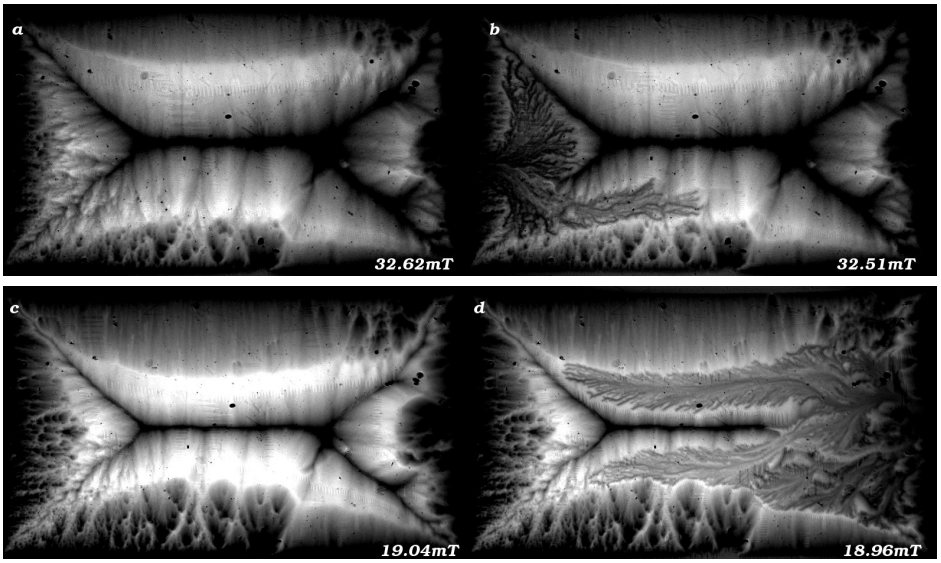

Figure 3.14: Magneto-optical image of dendritic avalanche into the bright d-line of the two-peak profile, at decreasing fields. The top images (a,b) are at T=8.5 K, and the bottom images (c,d) are at T=9 K

a two-peak profile where the slope has a sharp field minimum on the outside of the specimen. The Lorentz force will here point outwards of the sample, and an out-flux of vortices will begin when it exceeds the pinning force. The vortices moving towards the edges will cause heat dissipation, which may be enough to create a local instability at the edge of the film, triggering a flux avalanche [41] (e.g. figure 3.14 b and d). Since the density of vortices are highest at the bright discontinuity lines, the avalanche will advance mainly in this direction. It advances in a semi random way, creating the dendritic pattern. The avalanche creates so much heat that the core sometimes reach temperatures above T_c. The core is then field cooled back below T_c which gives a uniform distribution of vortices that can be seen as a uniform grey-colored core, e.g. figure 3.13 and 3.14 d.

3.4.3 Secondary avalanches crossing d-lines

In our experiments we also found a previously unexplained event, namely secondary avalanches that seems to start from the central d-line of a two-peak profiled structure. This can be observed in figures 3.15 and 3.16(closeup of 3.15) .

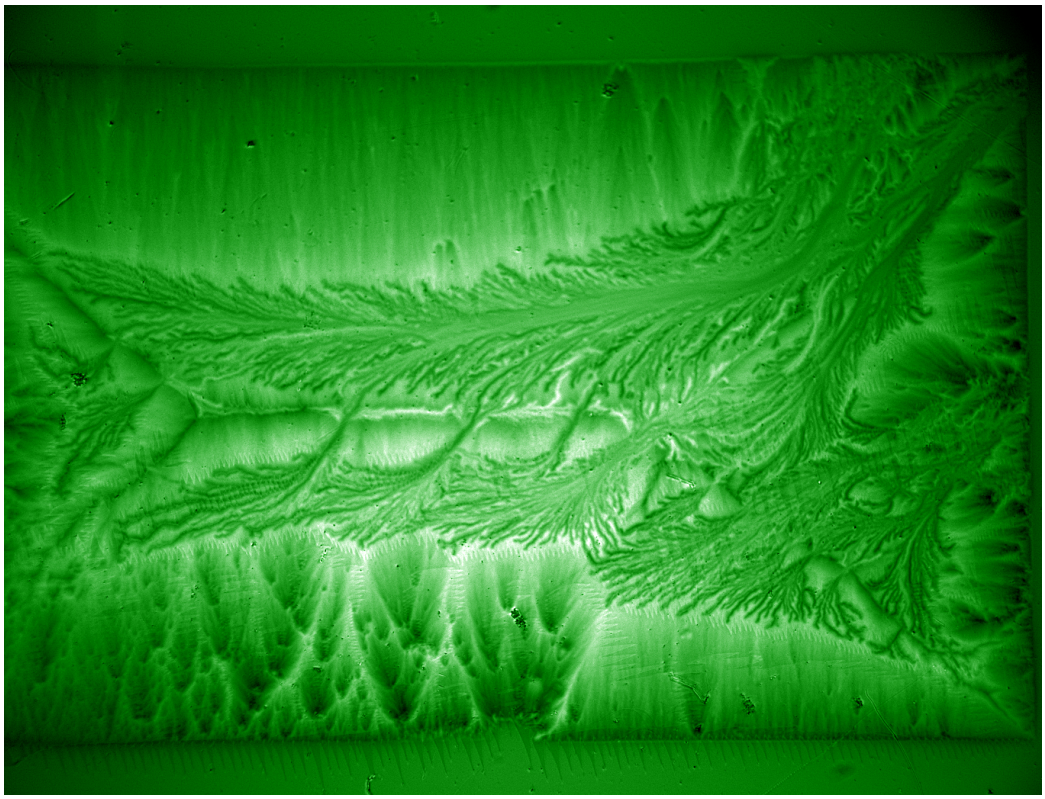

Figure 3.15: Magneto-optical image of NbN thin-film superconductor ZFC to T=9 K. The field was then slowly ramped up to B_{app}=34 mT, then slowly reduced to B_{app}=16.9 mT where the primary and secondary avalanches occurred

We observe dendritic avalanches both from the edge and from the d-line. The decreasing applied field on the edge cannot give a local instability in the center to start the secondary avalanches. We believe that the dendritic fingers from the primary avalanches starting on the edge approach the d-line and locally heat the surrounding area. This reduces the pinning force, and the Lorentz force will push the vortices towards the area with the lowest density, creating a local instability that triggers the secondary avalanches. The vortices will

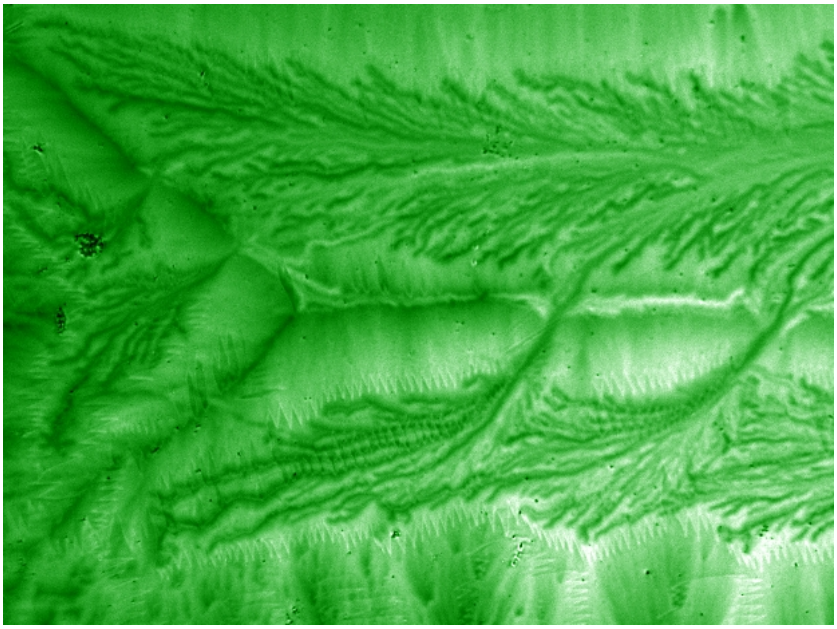

Figure 3.16: Close-up of figure 3.15, showing the secondary avalanches.

move to areas with lower density, meaning that it will either fill up the d-line, fill up the dendritic finger on the other side of the d-line or both.

Chapter 4

Concluding remarks

The goal of this thesis has been to study thermo-magnetic instability in superconductor thin-films, in as wide range of fields and temperatures as possible. The studies were conducted at both increasing and decreasing magnetic fields, with the magnetic flux range down-sampled into sufficiently small intervals. An automation procedure was developed in LabView to make the acquisition of data more precise and efficient. More than 32 000 images were acquired within the temperature range of 4 K to 10 K, which is an enormous amount of images for manual processing. An algorithm in Matlab for graphical recognition of magnetic flux avalanches was therefor developed. Another algorithm was developed to find upper and lower thresholds for increasing and decreasing applied fields.

Observations were made of a number of flux dynamic effects. We found that huge avalanches create enough heat for the temperature in the core of the avalanche to exceeded the critical temperature, meaning that the shielding current alter their path and the Lorentz force drive the avalanche into the area inside of the flux front. Another interesting observation was secondary avalanches triggered by a primary avalanche. It seems to be starting from the center zero-field d-line, as opposed to primary avalanches starting from the edge. Heat from the primary avalanche decreases the pinning sufficiently for the Lorentz force to move vortices toward the center d-line, which in some cases create local instabilities triggering secondary avalanches.

The thermo-magnetic instability threshold fields were used to construct a phase diagram, showing the fields as function of temperature. A hysteretic behaviour of the upper thresholds were observed for temperatures above 7 K, due to a higher absolute value of the critical current on the edge of the superconductor. This observation can be very important for the application of

superconductors, where thermo-magnetic instabilities are catastrophic. The qualitative explanation for threshold field hysteresis on the phase diagram is a solid ground for further quantitative study. With the tools developed in this thesis more experiments should be performed at different ramp rates to observe any correlation between ramp rate and threshold fields in different superconducting materials. The tools developed can with some modifications also be used for quantitative magneto-optics for exact reconstruction of current profiles.

Appendix A

LabView

CEFA4.vi

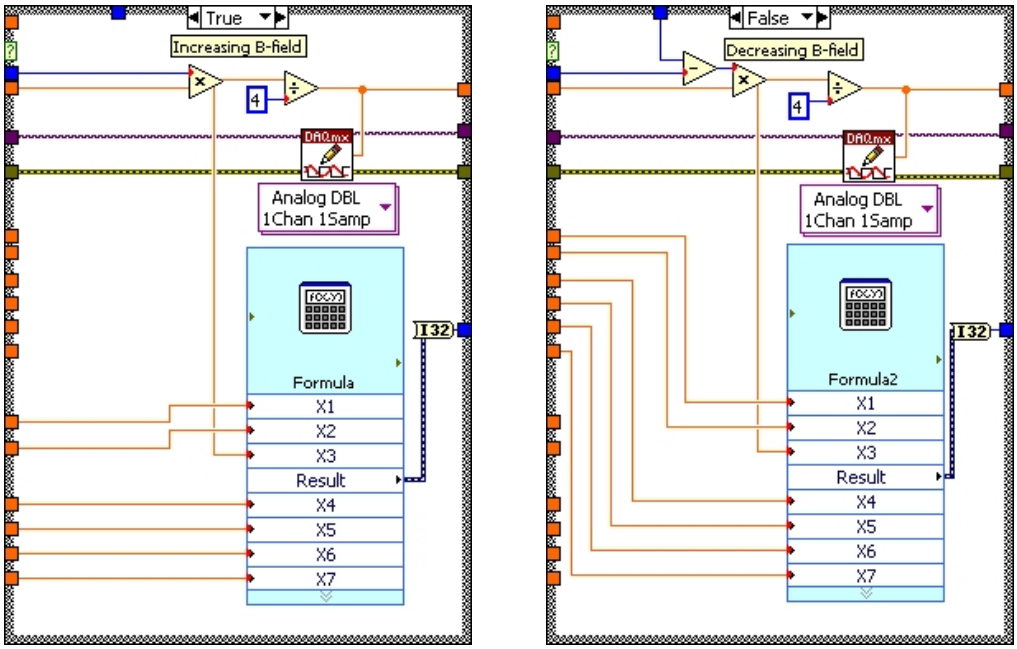

Figure A.1: CEFA4.vi true/false part

Imagecontrol.vi

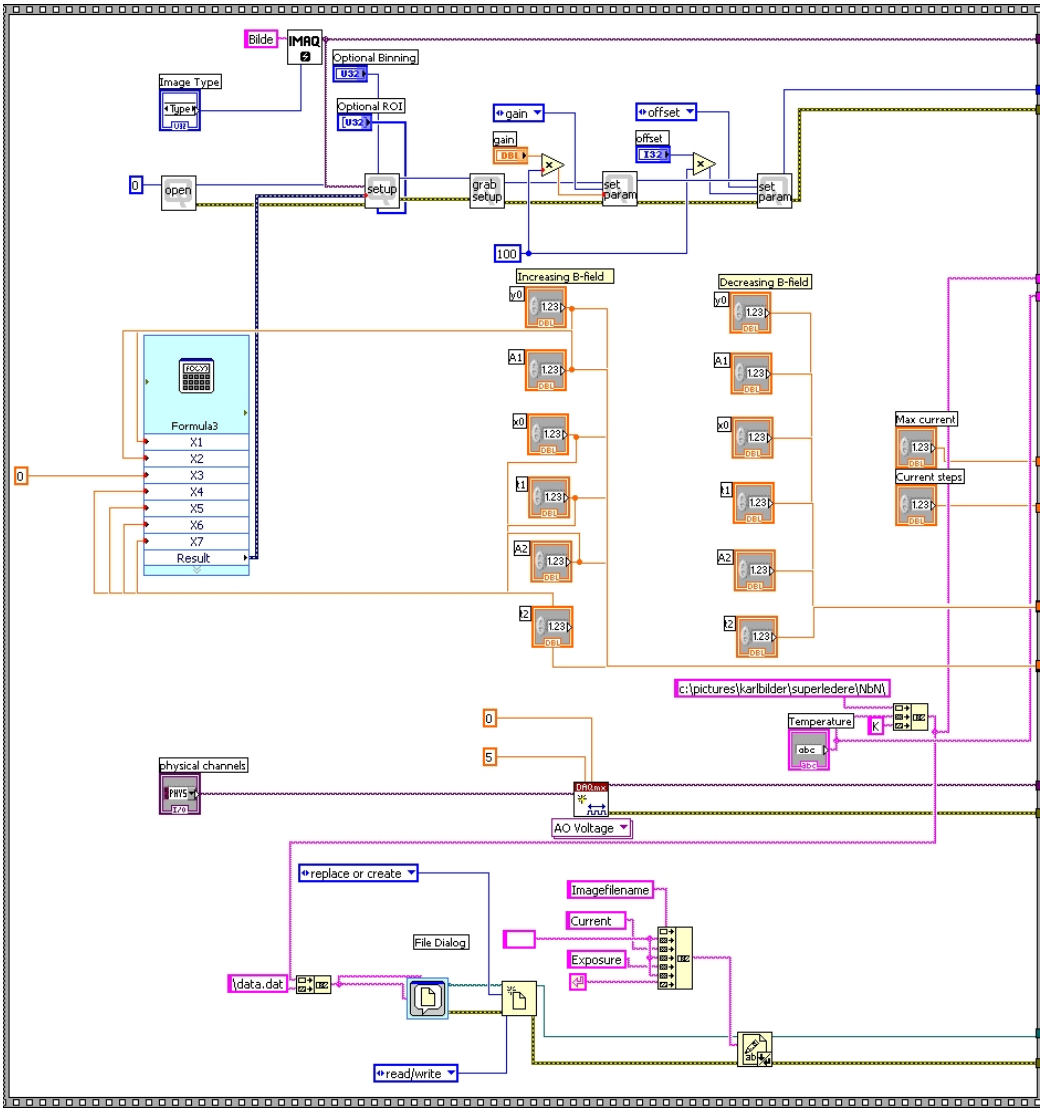

Figure A.2: CEFA4.vi, part 1 of 3, continues in figure A.3

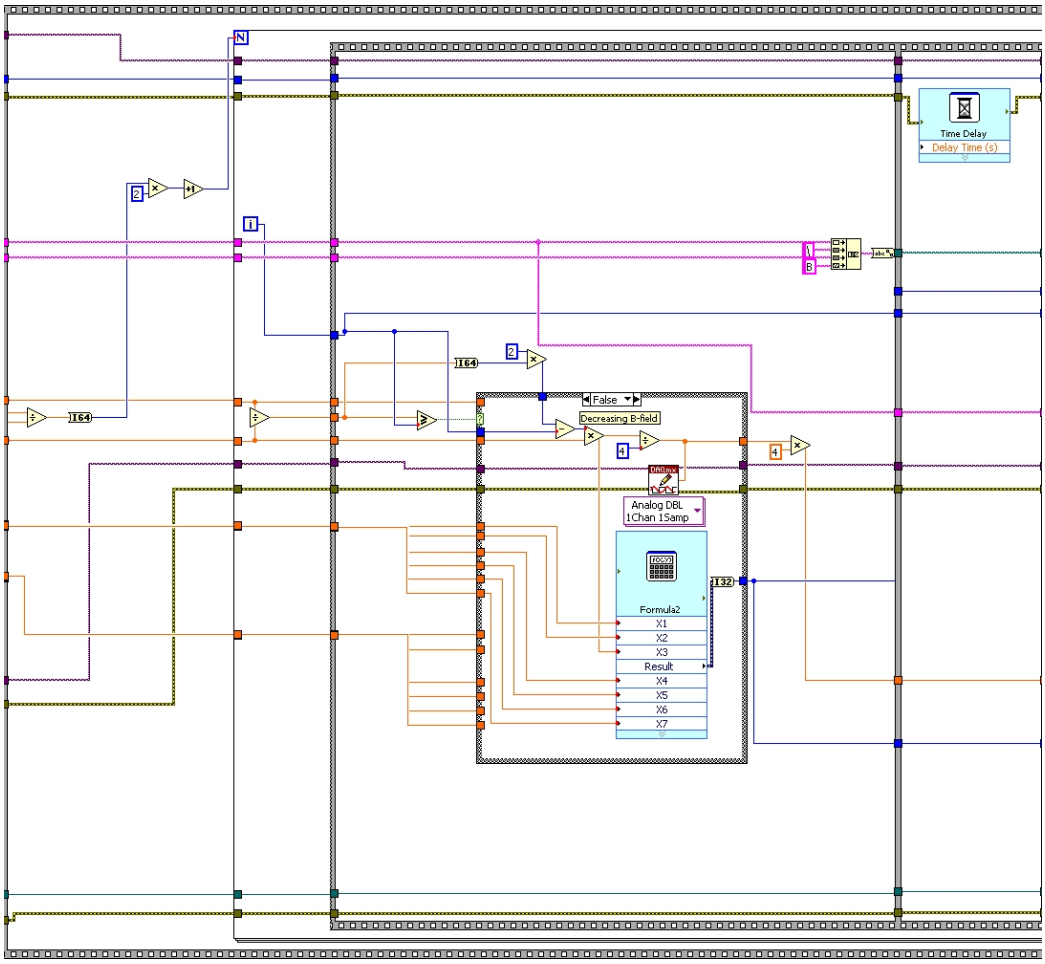

Figure A.3: CEFA4.vi part 2 of 3, continues in figure A.4

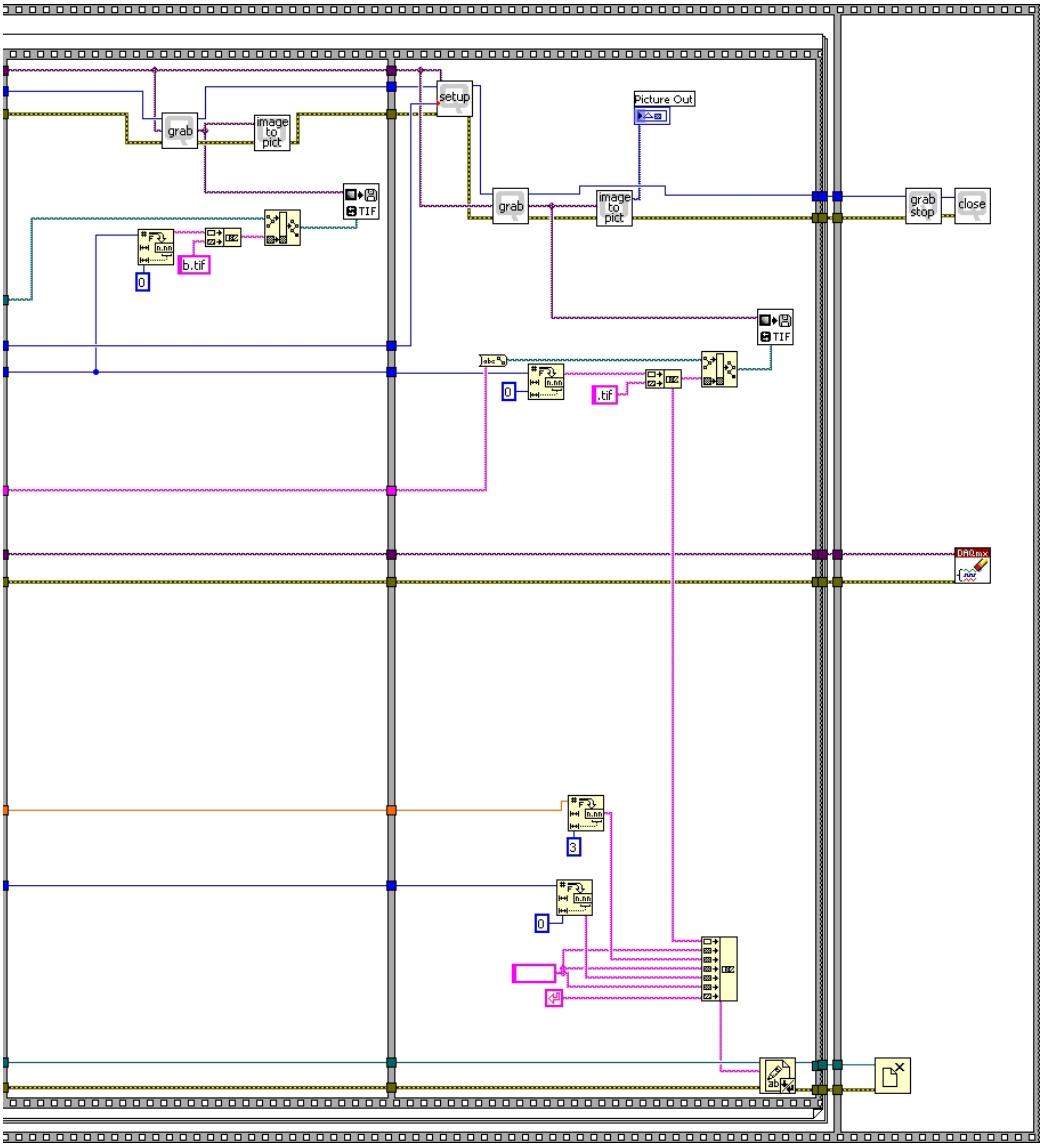

Figure A.4: CEFA4.vi part 3

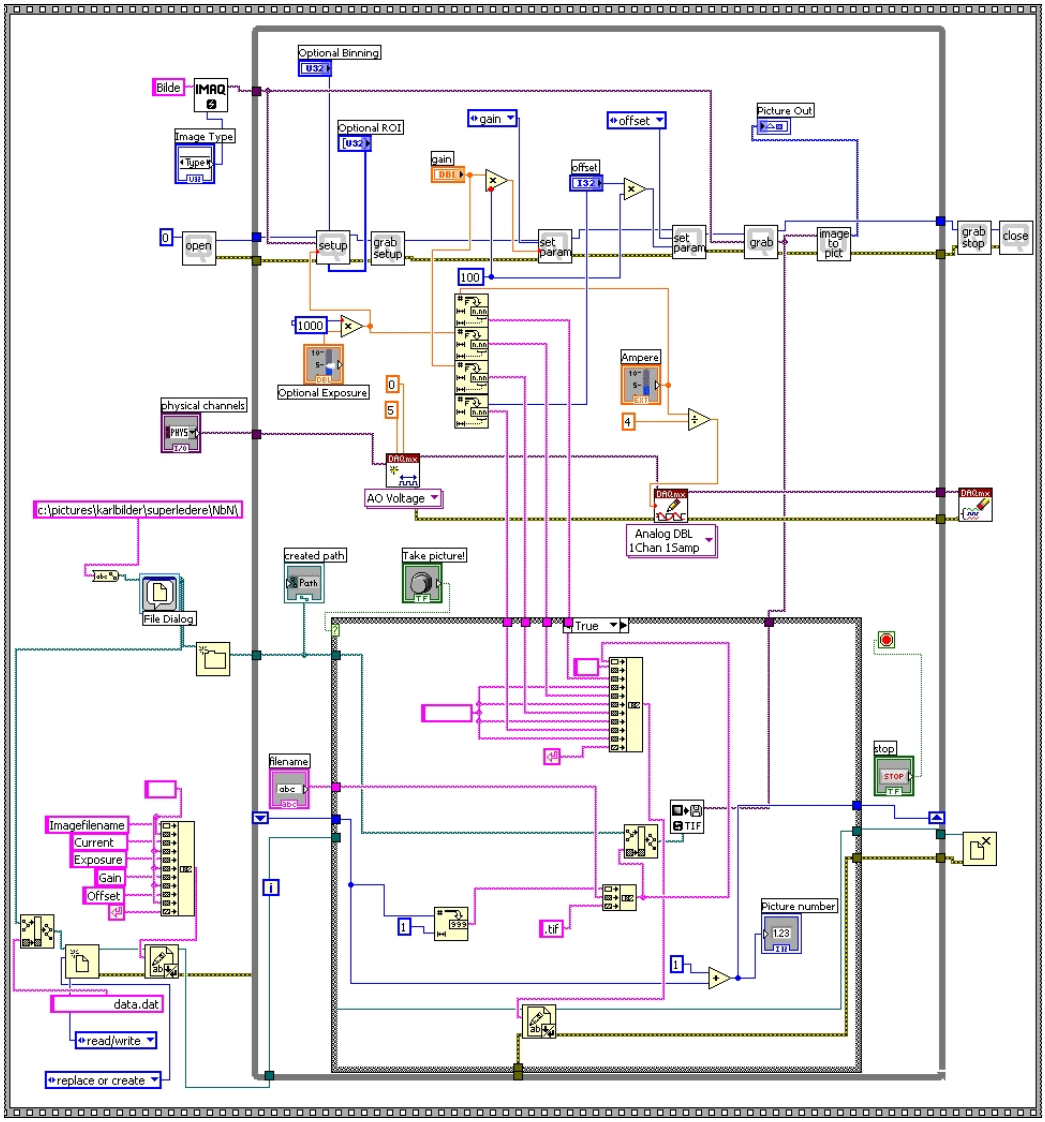

Figure A.5: Program developed for extracting data for Origin. Origin uses the data to find parameter which CEFA4.vi utilize to compute the exposure time

Appendix B

Matlab code

All of the following programs have been made in Matlab 7-5-0 (R2007b)

B.1 dendrites.m

```
function [] = difference(temp)
% Written by Karl Eliassen, AMCS, Deparment of Physics, UiO
temp = num2str(temp);
filenamepostfix= '.tif';
filenamepostfix2= 'b.tif';
mappe = ['image' temp 'K'];
mkdir(mappe);

for i=0:399
   number1 = int2str(i);
   number2 = int2str(i+1);

   filename1 = [temp 'K/' number1 filenamepostfix]; %generate name of
                                                    %first file to
                                                    %collect
   matrise1 = imread(filename1);     %collect first image
   matrise1 = matrise1(360:820,330:1120); %crop first image

   filename2 =[temp 'K/' temp 'B/' number2 filenamepostfix2];%generate name of
                                                            %second file to
                                                            %collect
   matrise2 = imread(filename2);     %collect second image
   matrise2 = matrise2(360:820,330:1120); %crop second image

   diff = matrise2-matrise1;         %subtract images

   %Now we do some calculations to remove noice and convert the
   %difference image in a best possible way from a 16bit into an 8bit
   %image.
   diff = diff.*uint16(diff>100);
   diff = diff - 100;
   diff = diff ./3;
   diff = uint8(diff);

   filename3 = [mappe '/image' number1 filenamepostfix]; %generate filename
                                                         %for the new image
```

```
   imwrite (diff, filename3);         %store image
end

for i=400:798
   number1 = int2str(i);
   number2 = int2str(i+1);

   filename1 = [temp 'K/' number1 filenamepostfix];  %generate name of
                                                     %first file to
                                                     %collect
   matrise1 = imread(filename1);      %collect first image
   matrise1 = matrise1(360:820,330:1120); %crop first image

   filename2 =[temp 'K/' temp 'B/' number2 filenamepostfix2];%generate name of
                                                            %second file to
                                                            %collect
   matrise2 = imread(filename2);      %collect second image
   matrise2 = matrise2(360:820,330:1120); %crop second image

   diff = matrise1-matrise2;          %subtract images

   %Now we do some calculations to remove noice and convert the
   %difference image in a best possible way from a 16bit into an 8bit
   %image.
   diff = diff.*uint16(diff>120);
   diff = diff - 120;
   diff = diff ./3;
   diff = uint8(diff);
   filename3 = [mappe '/image' number1 filenamepostfix]; %generate filename
                                                         %for the new image
   imwrite (diff, filename3);         %store image

end
```

B.2 finddend.m

```
function [] = finddend(temp, times, start)
     % Written by Karl Eliassen, AMCS Deparment og Physics, UiO
temp2 = temp;
temp = num2str(temp);
direc = ['image' temp 'Kb/' 'forskjell'];            %generate name
                                                     %for directory to
                                                     %store data
mkdir (direc);% make directory
     %Initialization of parameters, matrices etc. for later use
z  = 0;
zz = 0;
w  = 1;
C1 = 0;
thresholdend = zeros(4,1, 'double');
filenameprefix= 'image';
filenamepostfix= '.tif';
filenamepostfix2= '.out';
dend = zeros(800, 1, 'single');
square = zeros(20, 28, 'uint32');

threshold = temp2 * (708.8+0.00000000317*exp(temp2/0.34));
                                                     %noice threshold
                                                     %for increasing
                                                     %B-field.

for p=start:400 %loop for search of threshold fields at increasing B-field
    number = int2str(p-1);
    filename = [filenameprefix temp 'Kb/' filenameprefix number filenamepostfix];
                                                     %name of file to
                                                     %analyse.
    matrise1 = imread(filename);                     %read in imagefile

    for i=0:19
            A = (1+i*23):1:(23+i*23);                %Sets
                                                     %y-coordinates
                                                     %for square ixj

        for j=0:27
            B = (5+j*28):1:(32+j*28);%sets x-coordinates for square ixj
            square(i+1,j+1) = sum(sum(matrise1(A,B)));%Sums all values
                                                      %in square ixj
        end
    end

         %Here we want to see if two consecutive squares have
         %intensity higher than a threshold value calculated by
         %Origin, and if so say that the image holds a dendrite. Since
         %we only want to know if there is at least one dendrite here,
         %we derminate the search when we find one.
    square = square.*uint32(square>threshold);

    for i=1:19

        for j=1:27
            while dend(p,1) < 1 && C1 ~= 1

               if square(i,j)>0 && (square(i+1,j)>0 || square(i,j+1)>0)
                  dend(p,1) = 1;

               end
```

```
            C1 = 1;
        end
        C1 = 0;
    end
end

     %Finding the first image with dendrite(s); lower threshold
     %field at increasing B-field
if (dend(p,1)>0) && (z < w)
    thresholdend(1,1)= times*(p)/100;
    z = 1;
end

     %Finding the last image with dendrite(s); upper threshold
     %field at increasing B-field
if (dend(p,1)>0) && (z >= w)
    thresholdend(2,1)= times*(p)/100;
end
end


threshold = temp2 * (31.8 + 0.00226*exp(temp2/0.63)); %noice threshold
                                                      %for decreasing
                                                      %B-field

for p=401:800 %loop for search of threshold fields at decreasing B-field
    number = int2str(p-1);
    filename = [filenameprefix temp 'Kb/' filenameprefix number filenamepostfix];
                                                      %name of file to
                                                      %analyse
    matrise1 = imread(filename); %read in imagefile

    for i=0:19
        A = (1+i*23):1:(23+i*23);                     %Sets
                                                      %y-coordinates
                                                      %for square ixj

        for j=0:27
            B = (5+j*28):1:(32+j*28);                 %Sets
                                                      %x-coordinates
                                                      %for square ixj.
            square(i+1,j+1) = sum(sum(matrise1(A,B))); %Sums all
                                                       %values in
                                                       %square ixj
        end
    end


     %Here we want to see if two consecutive squares have
     %intensity higher than a threshold value calculated by
     %Origin, and if so say that the image holds a dendrite. Since
     %we only want to know if there is at least one dendrite here,
     %we derminate the search when we find one.
    square = square.*uint32(square>threshold);

    for i=1:19

        for j=1:27

            while dend(p,1) < 1 && C1 ~= 1

               if square(i,j)>0 && (square(i+1,j)>0 || square(i,j+1)>0)
```

```
                dend(p,1) = 1;

             end
             C1 = 1;
          end
          C1 = 0;
       end
    end


        %Finding the last image with dendrite(s); upper threshold
        %field at decreasing B-field
    if (dend(p,1)>0) && (zz < w)
       thresholdend(3,1)= times*(800.0 - p)/100;
       zz = 1;
    end

        %Finding the first image with dendrite(s); lower threshold
        %field at decreasing B-field
    if (dend(p,1)>0) && (zz >= w)
       thresholdend(4,1)= times*(800.0 - p)/100;
    end
end

thresholdend                                    %writes the threshold
                                                %fields to the screen.

    filename2 = ['image' temp 'K/forskjell/ruterb' filenamepostfix2];
                                                %generate name for
                                                %file to store data

    dlmwrite( filename2 ,dend );                %store data

    filename3 = ['image' temp 'K/forskjell/thresholdb' filenamepostfix2];
                                                %generate name for
                                                %file to store
                                                %threshold data
    dlmwrite( filename3 ,thresholdend );        %store threshold data
end
```

Bibliography

[1] Asle Sudbø Kristian Fossheim. *Superconductivity, physics and applications.* Wiley, 2005.

[2] M. Tinkham. *Introduction to Superconductivity.* McGraw-Hill, New York, 2nd ed. edition, 1996.

[3] H. Kamerlingh Onnes. The superconductivity of mercury. *Leiden Communications*, 12(119, 120b, 122b, 124c), 1911.

[4] H. Kamerlingh Onnes. The liquefication of helium. *Leiden Communications*, 11(108):168–185, 1908.

[5] J. G. Bednorz and K. A. Müller. Possible hightc superconductivity in the balacuo system. *Zeitschrift für Physik B Condensed Matter*, 64(2):189–193, June 1986.

[6] M. K. Wu, J. R. Ashburn, C. J. Torng, P. H. Hor, R. L. Meng, L. Gao, Z. J. Huang, Y. Q. Wang, and C. W. Chu. Superconductivity at 93 k in a new mixed-phase yb-ba-cu-o compound system at ambient pressure. *Phys. Rev. Lett.*, 58(9):908–910, Mar 1987.

[7] Tom Henning Johansen. Private collection.

[8] F. Kedves. Estimation of maximum electrical resistivity of high Tc superconducting ceramics by the meissner effect. *Solid State Communications*, 63:991–992, September 1987.

[9] R. Ochsenfeld W. Meissner. Ein neuer effekt bei eintritt der supraleitfähigkeit. *Naturwissenschaften*, 21(44):787–788, 1933.

[10] http://hoffman.physics.harvard.edu/research/SCintro.php.

[11] V. L. Ginzburg and L. D. Landau. *Zh. Eksperim. Teor. Fiz.*, 20:1064, 1950.

[12] H. London F. London. Supraleitung und diamagnetismus. *Physica*, Volume 2(Issues 1-12):341–354, 1935.

[13] Ruslan Prozorov. Equilibrium topology of the intermediate state in type-i superconductors of different shapes. *Physical Review Letters*, 98(25):257001, 2007.

[14] C.Poole, H.Farach, R.Creswick, and R.Prozorov. *Superconductivity.* Academic press, 2 edition, 2007.

[15] A. Abrikosov. Theoretical prediction of vortices in type ii superconductors. *Soviet Physics JETP 5*, 32:1442–1452, june 1957.

[16] Pål Erik Goa, Harald Hauglin, Michael Baziljevich, Eugene Il'yashenko, Peter L Gammel, and Tom H Johansen. Real-time magneto-optical imaging of vortices in superconducting nbse2. *Superconductor Science and Technology*, 14(9):729–731, 2001.

[17] C.Jooss et al. Magneto-optical studies of current distributions in high-t_c superconductors. *Reports on Progress in Physics*, 65(6):651–788, may 2002.

[18] Charles P. Bean. Magnetization of high-field superconductors. *Rev. Mod. Phys.*, 36(1):31–39, Jan 1964.

[19] Charles P. Bean. Rotational hysteresis loss in high-field superconductors. *Journal of Applied Physics*, 41(6):2482–2483, 1970.

[20] Y. B. Kim, C. F. Hempstead, and A. R. Strnad. Critical persistent currents in hard superconductors. *Phys. Rev. Lett.*, 9(7):306–309, Oct 1962.

[21] Y. B. Kim, C. F. Hempstead, and A. R. Strnad. Magnetization and critical supercurrents. *Phys. Rev.*, 129(2):528–535, Jan 1963.

[22] L. Ji, R. H. Sohn, G. C. Spalding, C. J. Lobb, and M. Tinkham. Critical-state model for harmonic generation in high-temperature superconductors. *Phys. Rev. B*, 40(16):10936–10945, Dec 1989.

[23] D. LeBlanc and M. A. R. LeBlanc. ac-loss valley in type-ii superconductors. *Phys. Rev. B*, 45(10):5443–5449, Mar 1992.

[24] Ming Xu, Donglu Shi, and Ronald F. Fox. Generalized critical-state model for hard superconductors. *Phys. Rev. B*, 42(16):10773–10776, Dec 1990.

[25] Ernst Helmut Brandt and Mikhail Indenbom. Type-ii-superconductor strip with current in a perpendicular magnetic field. *Phys. Rev. B*, 48(17):12893–12906, Nov 1993.

[26] E. H. Brandt, M. V. Indenbom, and A. Forkl. Type-ii superconducting strip in perpendicular magnetic field. *EPL (Europhysics Letters)*, 22(9):735–740, 1993.

[27] Ernst Helmut Brandt. Electric field in superconductors with rectangular cross section. *Phys. Rev. B*, 52(21):15442–15457, Dec 1995.

[28] R. G. Mints and A. L. Rakhmanov. Critical state stability in type-ii superconductors and superconducting-normal-metal composites. *Rev. Mod. Phys.*, 53(3):551–592, Jul 1981.

[29] V. V. Yurchenko, D. V. Shantsev, M. R. Nevala, I. J. Maasilta, K. Senapati, R. C. Budhani, and T. H. Johansen. Reentrant stability of superconducting films, 2007.

[30] DV Shantsev, AV Bobyl, YM Galperin, TH Johansen, and SI Lee. Size of flux jumps in superconducting films. *PHYSICAL REVIEW B*, 72(2), JUL 2005.

[31] E. Altshuler and T. H. Johansen. Colloquium: Experiments in vortex avalanches. *Rev. Mod. Phys.*, 76(2):471–487, Apr 2004.

[32] P. B. Alers. Structure of the intermediate state in superconducting lead. *Phys. Rev.*, 105(1):104–108, Jan 1957.

[33] P. Hansen, K. Witter, and W. Tolksdorf. Magnetic and magneto-optic properties of lead- and bismuth-substituted yttrium iron garnet films. *Phys. Rev. B*, 27(11):6608–6625, Jun 1983.

[34] P. E. Goa, H. Hauglin, A. A. F. Olsen, M. Baziljevich, and T. H. Johansen. Magneto-optical imaging setup for single vortex observation. *Review of Scientific Instruments*, 74(1):141–146, 2003.

[35] Arnold Sommerfeld. *Optics*, volume IV of *Lecture on theoretical physics*. Academic press, 1964. Translated by Otto Laporte and Peter A. Moldauer.

[36] K. Senapati, N. K. Pandey, Rupali Nagar, and R. C. Budhani. Normal-state transport and vortex dynamics in thin films of two structural polymorphs of superconducting NbN. *PHYSICAL REVIEW B*, 74(10), SEP 2006.

[37] I. A. Rudnev, D. V. Shantsev, T. H. Johansen, and A. E. Primenko. Avalanche-driven fractal flux distributions in nbn superconducting films. *Applied Physics Letters*, 87(4):042502, 2005.

[38] D. V. Denisov, A. L. Rakhmanov, D. V. Shantsev, Y. M. Galperin, and T. H. Johansen. Dendritic and uniform flux jumps in superconducting films. *Physical Review B (Condensed Matter and Materials Physics)*, 73(1):014512, 2006.

[39] D. V. Denisov, D. V. Shantsev, Y. M. Galperin, Eun-Mi Choi, Hyun-Sook Lee, Sung-Ik Lee, A. V. Bobyl, P. E. Goa, A. A. F. Olsen, and T. H. Johansen. Onset of dendritic flux avalanches in superconducting films. *Physical Review Letters*, 97(7):077002, 2006.

[40] E. Altshuler, T. H. Johansen, Y. Paltiel, Peng Jin, K. E. Bassler, O. Ramos, Q. Y. Chen, G. F. Reiter, E. Zeldov, and C. W. Chu. Vortex avalanches with robust statistics observed in superconducting niobium. *Phys. Rev. B*, 70(14):140505, Oct 2004.

[41] Ruslan Prozorov, Daniel V. Shantsev, and Roman G. Mints. Collapse of the critical state in superconducting niobium. *Physical Review B*, 74:220511, 2006.